AGU PUBLICATIONS

JGR

Journal of Geophysical Research: Atmospheres

RESEARCH ARTICLE
10.1002/2014JD021673

Key Points:
- Development of a remotely sensing seasonal vegetation-based PDSI
- Global land wetting due to increased precipitation and ENSO for past 30 years
- PDSI values are sensitive to the parameterizations for potential evaporation

Correspondence to:
H. Yan,
yanhaon@hotmail.com

Citation:
Yan, H., S.-Q. Wang, H.-Q. Lu, Q. Yu, Z.-C. Zhu, R. B. Myneni, Q. Liu, and H. H. Shugart (2014), Development of a remotely sensing seasonal vegetation-based Palmer Drought Severity Index and its application of global drought monitoring over 1982–2011, *J. Geophys. Res. Atmos.*, *119*, doi:10.1002/2014JD021673.

Received 25 FEB 2014
Accepted 25 JUL 2014
Accepted article online 29 JUL 2014

Development of a remotely sensing seasonal vegetation-based Palmer Drought Severity Index and its application of global drought monitoring over 1982–2011

Hao Yan[1,2], Shao-Qiang Wang[3], Hou-Quan Lu[1], Qin Yu[2], Zai-Chun Zhu[4,5], Ranga B. Myneni[6], Qiang Liu[7], and Herman H. Shugart[2]

[1]National Meteorological Center, China Meteorological Administration, Beijing, China, [2]Environmental Sciences Department, University of Virginia, Charlottesville, Virginia, USA, [3]Institute of Geographic Sciences and Natural Resources Research, Chinese Academy of Sciences, Beijing, China, [4]State Key Laboratory of Remote Sensing Science, Institute of Remote Sensing and Digital Earth, Chinese Academy of Sciences, Beijing, China, [5]Center for Applications of Spatial Information Technologies in Public Health, Beijing, China, [6]Department of Earth and Environment, Boston University, Boston, Massachusetts, USA, [7]College of Global Change and Earth System Science, Beijing Normal University, Beijing, China

Abstract Vegetation effects are currently disregarded in Palmer Drought Severity Index (PDSI), and the sensitivity of PDSI to the choice of potential evaporation (E_P) parameterization is often a concern. We developed a revised self-calibrating PDSI model that replaces E_P with leaf area index-based total evapotranspiration (ARTS E_0). It also included a simple snowmelt module. Using a unique satellite leaf area index data set and climate data, we calculated and compared ARTS E_0, three other types of E_P (i.e., Thornthwaite E_{P_Th}, Allen E_{P_Al}, and Penman-Monteith E_{P_PM}), and corresponding PDSI values (i.e., PDSI_ARTS, PDSI_Th, PDSI_Al, and PDSI_PM) for the period 1982–2011. The results of PDSI_ARTS, PDSI_Al, and PDSI_PM show that global land became wetter mainly due to increased precipitation and El Niño–Southern Oscillation (ENSO) effect for the period, which confirms the ongoing intensification of global hydrologic cycle with global temperature increase. However, only PDSI_Th gave a trend of global drying, which confirms that PDSI_Th overestimates the global drying in response to global warming; i.e., PDSI values are sensitive to the parameterizations for E_p. Thus, ARTS E_0, E_{P_Al}, and E_{P_PM} are preferred to E_{P_Th} in global drought monitoring. In short, global warming affects global drought condition in two opposite ways. One is to contribute to the increases of E_P and hence drought; the other is to increase global precipitation that contributes to global wetting. These results suggest that precipitation trend and its interaction with global warming and ENSO should be given much attention to correctly quantify past and future trends of drought.

1. Introduction

Drought is an extreme climate event that often causes severe stress on environmental processes and social-economic activities. Meteorological drought is characterized by below-normal precipitation over months or even years. When drought depletes the soil water, it affects crop production and plant growth, which is called agricultural drought. Numerous drought indices have been developed to quantify the complicated drought processes [*Heim*, 2002]. Among them, the Palmer Drought Severity Index (PDSI) [*Palmer*, 1965] has been widely used to measure cumulative departure in surface water balance and to quantify dry and wet periodicity at regional to global scales [*Heim*, 2002; *Dai et al.*, 2004; *Dai*, 2011; *van der Schrier et al.*, 2013; *Sheffield et al.*, 2012]. PDSI takes antecedent precipitation, moisture supply, and moisture demand into account by using a two-layered soil-water balance model. According to PDSI value, relative dry conditions are classified into 11 classes from extremely wet to extreme drought (Table 1) [*Palmer*, 1965].

Compared with drought indices from precipitation-based models such as precipitation anomaly index, the PDSI model and its improved variants have the merit of considering the interactive effects of potential evaporation and precipitation based on Thornthwaite's water balance model [*Thornthwaite*, 1948]. Evaluation with observed soil moisture and river flow has demonstrated PDSI's potential in drought monitoring [*Dai et al.*, 2004]. The simple structure of model enables wide applications [*Heim*, 2002]. Concomitantly, it has been criticized for an absence of some physical processes. *Alley* [1984] noted concerns about modeling

Table 1. Classification of Dry and Wet Degree as Defined by *Palmer* [1965] PDSI Index

PDSI	Class	PDSI	Class
4.0≤PDSI	Extremely wet	−1.0 to −0.5	Incipient drought
3.0 to 4.0	Very wet	−2.0 to −1.0	Mild drought
2.0 to 3.0	Moderately wet	−3.0 to −2.0	Moderate drought
1.0 to 2.0	Slightly wet	−4.0 to −3.0	Severe drought
0.5 to 1.0	Incipient wet spell	PDSI≤−4.0	Extreme drought
−0.5 to 0.5	Near normal		

soil moisture, runoff, actual evapotranspiration on a monthly temporal scale including neglect of seasonal or interannual changes in vegetation cover and root development, and of the effects of snowmelt or frozen ground. Calibration coefficients and the temperature-alone-based Thornthwaite potential evaporation (1948) formula have also been questioned [*Karl*, 1986; *Guttman et al.*, 1992; *Sheffield et al.*, 2012]. Although *Palmer* [1965] attempted to develop a drought index that could be compared among different locations and seasons of a year, the empirical constants used in the original PDSI model were calculated from nine climatic divisions located in the Midwestern United States. This limits its spatial comparability [*Alley*, 1984; *Karl*, 1986; *Guttman et al.*, 1992; *Wells et al.*, 2004] and even leads to unrealistic results when the PDSI is applied beyond these conditions not found in these nine regions [*Palmer*, 1965].

To improve the PDSI model, *Wells et al.* [2004] developed a self-calibrating PDSI (scPDSI) that automatically calibrates itself at any location by using dynamically computed values instead of using the empirical constants associated with fixed climatic divisions. scPDSI has been successfully applied to spatial comparison of drought at sites or regions around the world [*Wells et al.*, 2004; *Sheffield et al.*, 2012; *van der Schrier et al.*, 2013]. Because the Thornthwaite-temperature model (1948) overestimates the potential evaporation as air temperature increases [*Lockwood*, 1999], it induces an unrealistic increase in PDSI drought frequency [*Burke et al.*, 2006] and drought intensity [*Sheffield et al.*, 2012]. Thus, in revised PDSI models, Thornthwaite E_P has been replaced with Penman-Montheith-type E_P models [*Shuttleworth*, 1993; *Allen et al.*, 1994] to take into account radiation, wind speed, and temperature [*Burke et al.*, 2006; *Sheffield et al.*, 2012; *van der Schrier et al.*, 2013]. However, the sensitivity of PDSI model to the parameterization of E_P has been debated [*Dai*, 2011; *van der Schrier et al.*, 2011; *Sheffield et al.*, 2012]. *Dai* [2011] and *van der Schrier et al.* [2011] found that PDSI values are very similar even when different E_P estimates are used in PDSI models; this finding is disputed by *Sheffield et al.* [2012].

Another issue in recent PDSI-based drought studies [*Dai et al.*, 2004; *Dai*, 2011; *van der Schrier et al.*, 2013; *Sheffield et al.*, 2012] is that they unintentionally ignore the impact of precipitation on the trend of global land drought. Additionally, the vegetation effect on the PDSI that concerned *Alley* [1984] has not been completely addressed in global drought monitoring. Using a self-calibrating method, *van der Schrier et al.* [2013] developed a new PDSI model, which considered more physical processes including seasonal snowpack dynamics along with actual vegetation cover but with no seasonal changes.

Recently, an air-relative-humidity-based, two-source, evapotranspiration model (ARTS) [*Yan et al.*, 2012] has been developed to simulate the surface-energy balance, soil-water balance, and environmental constraints on evapotranspiration (E). It incorporates remotely sensed leaf area index (LAI) into a simple canopy conductance model (G_c) for calculating canopy transpiration from the G_c-based Penman-Monteith (PM) E equation. Total evapotranspiration (ARTS E_0), the sum of the canopy transpiration and soil evaporation, is corrected for soil water stress by using the Thornthwaite's water balance model [*Thornthwaite*, 1948]. The ARTS E_0 module has been successfully applied to site E estimates [*Yan et al.*, 2012] and diagnostic analysis of interannual variation of global land evapotranspiration as well as the impact of El Niño–Southern Oscillation (ENSO) [*Yan et al.*, 2013]. This informs the coupling ARTS E_0 with self-calibrating PDSI model to take advantage of seasonal vegetation information in response to *Alley's* [1984] concerns.

In this paper, we present a new self-calibrating PDSI model (ARTS PDSI) that includes a simple snowmelt and accumulation module, and a seasonal vegetation-based total evapotranspiration module. As Climate Research Unit (CRU) data sets with strict quality control have been widely used in PDSI drought monitoring [*Dai*, 2011; *van der Schrier et al.*, 2011], the latest version of CRU precipitation data is used in this study. Global Inventory Modeling and Mapping Studies (GIMMS) leaf area index (LAI) data as a unique data spanning from 1982 to 2011 [*Zhu et al.*, 2013] are used to represent actual vegetation in the ARTS PDSI model.

The ARTS PDSI model is described and discussed below in five sections: (1) model introduction; (2) description of remotely sensing vegetation LAI and meteorological data sets and data preprocessing methods; (3) diagnostic analysis of interannual variations of global drought over 1982–2011 and impact of global land precipitation; (4) assessment of global drought by comparison with PDSI values, associated E_P values, and previous studies to answer the concern of PDSI sensitivity to different E_P parameterizations; and (5) discussion of the potential use of the ARTS PDSI model for global drought monitoring.

2. Self-Calibrating PDSI Model Driven With ARTS E_0

2.1. ARTS E_0 Module

Based on "big leaf" plant canopy assumption, the Penman-Monteith model implementations [*Monteith*, 1965] typically calculate surface conductance directly from LAI regardless of soil evaporation [*Allen*, 1998; *Cleugh et al.*, 2007]. *Allen* [1998] showed that surface conductance also should include the contribution of soil evaporation especially where there is scarce vegetation. This soil evaporation problem also holds for recent vegetation-based scPDSI model [*van der Schrier et al.*, 2013], which adopts the Penman-Monteith big leaf E_P. In contrast, the ARTS E_0 module [*Yan et al.*, 2012] calculates both plant transpiration (E_c) and soil evaporation (E_s) assuming plenty of soil water availability:

$$E_0 = E_c + E_s \tag{1}$$

Similarly, the available energy A is partitioned to the soil part (A_s) and canopy part (A_c):

$$A_s = A\exp(-k_A L_{ai}) \tag{2}$$

$$A_c = A - A_s, \tag{3}$$

where A_c and A_s are the parts of the available energy (A) that are absorbed by the canopy and by the soil, respectively, and k_A equals 0.6 [*Impens and Lemeur*, 1969]. A is set to the net radiation R_n, because the soil heat flux G can be ignored in the calculation of E on daily and monthly scales [*Allen*, 1998].

The canopy transpiration (E_c) model is calculated from the modified Penman-Monteith model with input of the canopy-absorbed available energy (A_c) and canopy conductance (G_c):

$$E_c = \frac{\Delta A_c + \rho C_p D G_a}{\Delta + \gamma(1 + G_a/G_c)}, \tag{4}$$

$$G_c = g_{s\,max} \times R_h \times L_{ai}, \tag{5}$$

where A_c is the available energy absorbed by the canopy, Δ is the gradient of the saturated vapor pressure to air temperature, γ is the psychrometric constant, ρ is the density of air, C_p is the specific heat of air at constant pressure, G_a is the aerodynamic conductance, G_c is the canopy conductance accounting for transpiration from the vegetation, and $D = e_s - e_a$ is the vapor pressure deficit of the air, in which e_s is the saturation water vapor pressure at air temperature and e_a is the actual water vapor pressure, R_h is the relative humidity, and g_{smax} is the maximum stomatal conductance assumed to have a value of 12.2 mm s^{-1} [*Kelliher et al.*, 1995].

The soil evaporation (E_s) equation is modified from an air-relative-humidity-based model of evapotranspiration (ARM-ET) [*Yan and Shugart*, 2010]:

$$E_s = 1.35 R_h \frac{\Delta A_s}{\Delta + \gamma}, \tag{6}$$

The ARM-ET model scales the *Priestley and Taylor* [1972] equilibrium evaporation to actual E by using R_h as a complementary relationship coefficient.

2.2. A Snowmelting and Accumulation Module

According to a temperature threshold of 0°C, precipitation P_r is first divided into rainfall and snowfall; snowfall is then added to the snowpack (S_{now}). Snowmelt is calculated from snowpack using a temperature-

based snowmelt function. The water supply P, defined as the sum of rainfall and snowmelt, is used to substitute for P_r to drive the self-calibrating PDSI model:

$$P = R_{\text{ain}} + S_{\text{now}} \times S_{\text{f}} \tag{7}$$

$$S_{\text{f}} = \begin{cases} 0 & \text{if } T \le 0^{\circ}\text{C} \\ 0.2T & \text{if } 0^{\circ}\text{C} < T \le 5^{\circ}\text{C} \\ 1 & \text{if } T > 5^{\circ}\text{C} \end{cases} \tag{8}$$

where P is the water input (mm mo^{-1}) including rainfall (R_{ain}) and snowmelt, S_{f} is the snowmelting factor, and T is the air temperature (°C).

2.3. ARTS PDSI Model

The ARTS E_0 represents total evapotranspiration for a well-watered surface. The self-calibrating PDSI model [*Wells et al.*, 2004] included to correct E_0, similarly to traditional E_{P}, and produce actual E as well as PDSI. The soil water balance module, as a core of PDSI model, is widely applied to correct E_{P} [*Thornthwaite and Mather*, 1955; *Allen*, 1998]. The PDSI model differs from original ARTS E model [*Yan et al.*, 2012] in that it uses a two-layer soil water balance model. The ARTS E model adopts a single-layer soil water balance model of *Thornthwaite and Mather* [1955].

The ARTS PDSI model couples a self-calibrating PDSI model [*Wells et al.*, 2004] with the ARTS E_0 module and snowmelting module to account for the effects of calibration coefficients, seasonal vegetation, and snowmelting. The ARTS E_0 module and the simple snowmelting module in section 2.1 are adopted from ARTS E model [*Yan et al.*, 2012]. The self-calibrating PDSI model [*Wells et al.*, 2004] used in this study can be found in Appendix A (Calculation of Self-Calibrating PDSI model). Its calibration interval used in the present study covers the entire data period of 1982–2011. The water supply P, defined as the sum of rainfall and snowmelt derived from the simple snowmelting module (see equation (8)), drives self-calibrating PDSI model instead of the more usual P_r.

3. Data Sets and Preprocessing

3.1. MERRA Reanalysis Data

Modern-Era Retrospective Analysis for Research and Applications (MERRA) is a 35 year reanalysis product that covers the modern satellite era from 1979 to 2013. It is generated by using a new version of the National Aeronautics and Space Administration (NASA) Goddard Earth Observing System Data Assimilation System version 5. MERRA assimilates the NASA modern Earth Observing System suite of satellite observations in a climate framework focusing on historical analyses of the hydrological cycle [*Rienecker et al.*, 2011]. It is expected to represent meteorological and hydrological processes better than existing reanalysis products. As an observational analysis, MERRA produces a temporally and spatially consistent analyses of atmosphere, land surface, and ocean surface variables at a horizontal resolution (0.5° latitude × 0.67° longitude) that have been successfully used for investigating hydrological variability [*Reichle et al.*, 2011; *Yi et al.*, 2011; *Yan et al.*, 2013].

3.2. CRU Precipitation Data

The current CRU time series 3.21 monthly climate data set at 0.5° × 0.5° resolution over the period 1901–2012 was produced by the Climate Research Unit (CRU) at the University of East Anglia. It comprises six mostly independent climate elements: mean temperature, diurnal temperature range, precipitation, wet-day frequency, vapor pressure, and cloud cover [*New et al.*, 2000; *Harris et al.*, 2013]. CRU data sets have been widely used in recent studies of global drought and hydrology cycle [*Gerten et al.*, 2008; *Dai*, 2011; *Sheffield et al.*, 2012; *van der Schrier et al.*, 2013]. The monthly precipitation data for the period 1982–2011 were adopted in this study as model forcings.

3.3. GIMMS and Global Land Surface Satellite Leaf Area Index Data

The latest global LAI and Fraction of Photosynthetically Active Radiation absorbed (FPAR) data sets (LAI3g and FPAR3g), at 15 day temporal intervals and 8 km spatial resolutions for the period from July 1981 to

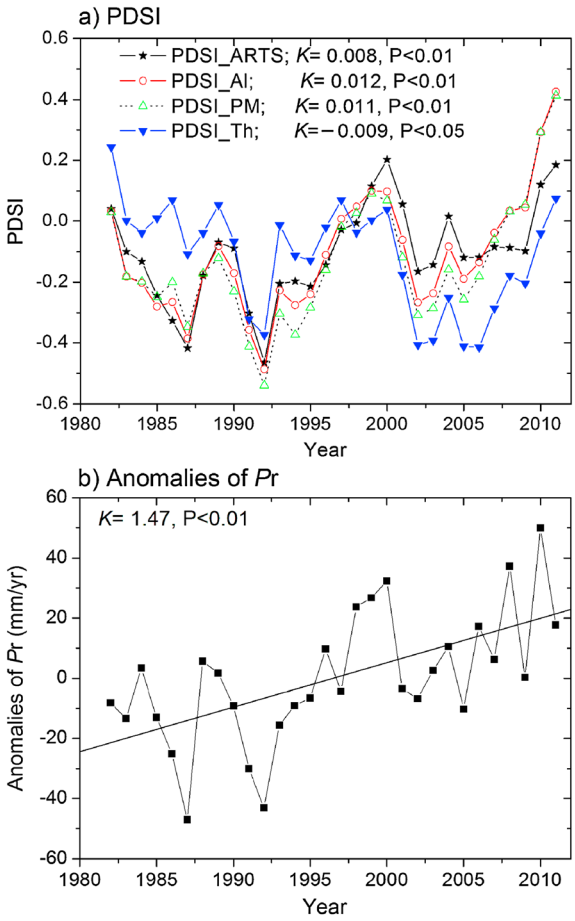

Figure 1. Time series of globally averaged annual anomalies of (a) self-calibrating PDSI_ARTS, PDSI_AI, PDSI_PM, and PDSI_Th and (b) precipitation P_r over 1982–2011.

December 2011, are generated from advanced very high resolution radiometer (AVHRR) GMMS NDVI3g data set using an Artificial Neural Network (ANN) model [*Zhu et al.*, 2013]. The ANN model for generating the LAI/FPAR data set was trained with overlapping GIMMS NDVI3g and best quality Moderate Resolution Imaging Spectroradiometer (MODIS) LAI/FPAR products for the period from 2000 to 2009. The trained ANN model was then used to generate LAI3g and FPAR3g data set using GIMMS NDVI3g data for the remaining period. The unique 30 year satellite LAI/FPAR data set have been used in researches of global land evapotranspiration as well as the impact of ENSO [*Yan et al.*, 2013], gross primary productivity in Asia [*Ichii et al.*, 2013], and evaluation of land surface models in reproducing satellite-derived LAI [*Anav et al.*, 2013] and solar radiation partitioning scheme [*Wang et al.*, 2013].

The Global Land Surface Satellite (GLASS) LAI product, another global LAI product at a temporal resolution of 8 days and a geographic resolution of 0.05° available from 1982 to 2012, was obtained from the Center for Global Change Data Processing and Analysis of Beijing Normal University (http://www.bnu-datacenter.com/). Using General Regression Neural Networks trained by the fusion of the MODIS and CYCLOPES LAI products during the 2001–2003 period, the LAI product was generated from AVHRR reflectance before 1999 and from MODIS land surface reflectance (MOD09A1) after 2000, respectively. As it is spatially complete and temporally continuous, the GLASS LAI product is ideal for global change and climate studies [*Zhao et al.*, 2013].

3.4. ISLSCP II Global Gridded Soil Data

Global 1° gridded data set of 18 selected soil parameters including maximum soil available water content (M_{awc}) for a soil depth of 0–150 cm, downloaded from the Oak Ridge National Laboratory Distributed Active Archive Center (ORNL DAAC) (http://daac.ornl.gov/) by this study, was developed by the International Satellite Land Surface Climatology Project (ISLSCP) Initiative II project based on the International Geosphere-Biosphere Programme–Data and Information Services soil data [*Hall et al.*, 2006].

3.5. Data Preprocessing

All model forcing data including LAI, MERRA reanalysis meteorological data, CRU precipitation data, and ISLSCP II maximum soil available water content data were averaged to a $1° \times 1°$ grid resolution. GIMMS LAI and MERRA reanalysis meteorological data (i.e., net radiation, air temperature, specific humidity, wind speed, roughness length, and displacement height) were then applied to driving the ARTS E_0 module on a monthly time scale. ARTS E_0 and CRU precipitation also drove the ARTS PDSI model with aid of ISLSCP II maximum soil available water content data.

To compare the sensitivity of PDSI model to different parameterizations of E_P, we also calculated more PDSI values from the ARTS PDSI model but forced with the Allen reference E_{p_re} [*Allen*, 1998], Penman-Monteith

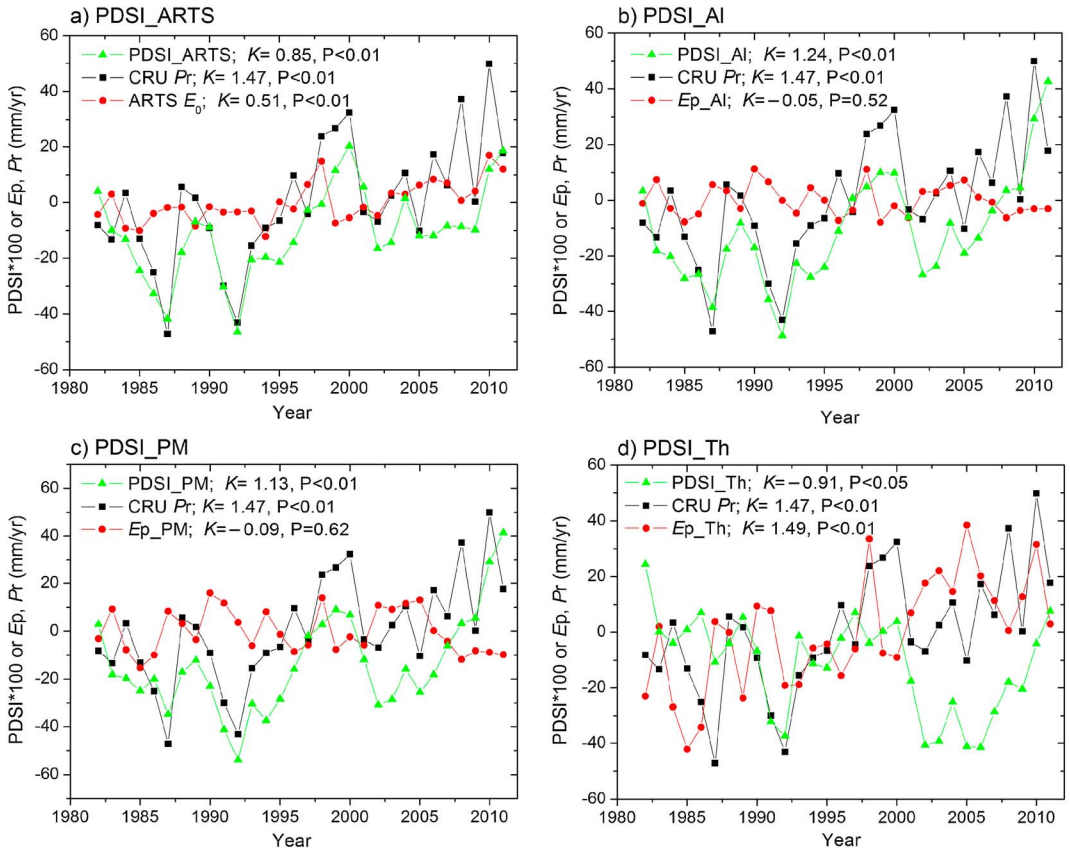

Figure 2. Comparisons of annual anomalies of self-calibrating (a) PDSI_ARTS, (b) PDSI_AI, (c) PDSI_PM, and (d) PDSI_Th with CRU P_r and corresponding E_0 (or E_P) from 1982 to 2011.

E_{P_PM} [*Shuttleworth*, 1993], and Thornthwaite E_{P_Th} [*Thornthwaite*, 1948] instead of ARTS E_0. The three types of E_P were calculated from the MERRA reanalysis meteorological data for the same period 1982 to 2011. Their explicit introduction can be found in Appendix B.

3.6. Two Published PDSI Data Sets

Two available PDSI data sets [*Dai*, 2011; *van der Schrier et al.*, 2013] were used in this study. The PDSI_ Dai data set [*Dai*, 2011] is a monthly self-calibrating PDSI [*Wells et al.*, 2004] product at a 2.5° × 2.5° resolution for period 1850–2010 (http://www.cgd.ucar.edu/cas/catalog/climind/pdsi.html), which uses the Penman-Monteith potential evapotranspiration recommended by *Shuttleworth* [1993] and numerous sources of forcing data.

The PDSI_Schrier data set [*van der Schrier et al.*, 2013] is also a monthly scPDSI [*Wells et al.*, 2004] product with a 0.5° × 0.5° resolution (http://badc.nerc.ac.uk/browse/badc/cru/data/cru_ts/PDSI) calculated from the CRU time series 3.10.01 data sets for period 1901–2009. It revises the traditional scPDSI model to include the effect of snowmelting process and the actual vegetation by using the Penman-Monteith parameterization for E_P [*Monteith*, 1965; *Allen et al.*, 1994].

4. Results

4.1. Interannual Variations of Global Land PDSI, E_P, and P_r

Annual average PDSI_ARTS (Figure 1) shows an increase of 0.08 per decade from 1982 to 2011; i.e., global land significantly became more humid for the period. PDSI_AI and PDSI_PM (Figure 1a) also had a similar wetting trend. However, PDSI_Th had an opposite trend; i.e., PDSI_Th decreased by −0.09 per 10 years indicating global land became much drier during the same period. The same CRU P_r data were ingested by PDSI models as water supply. Figure 1b shows that annual CRU P_r over global land tended to increase by 14.7 mm per 10 years during the past 30 years; i.e., more precipitation poured down into the terrestrial

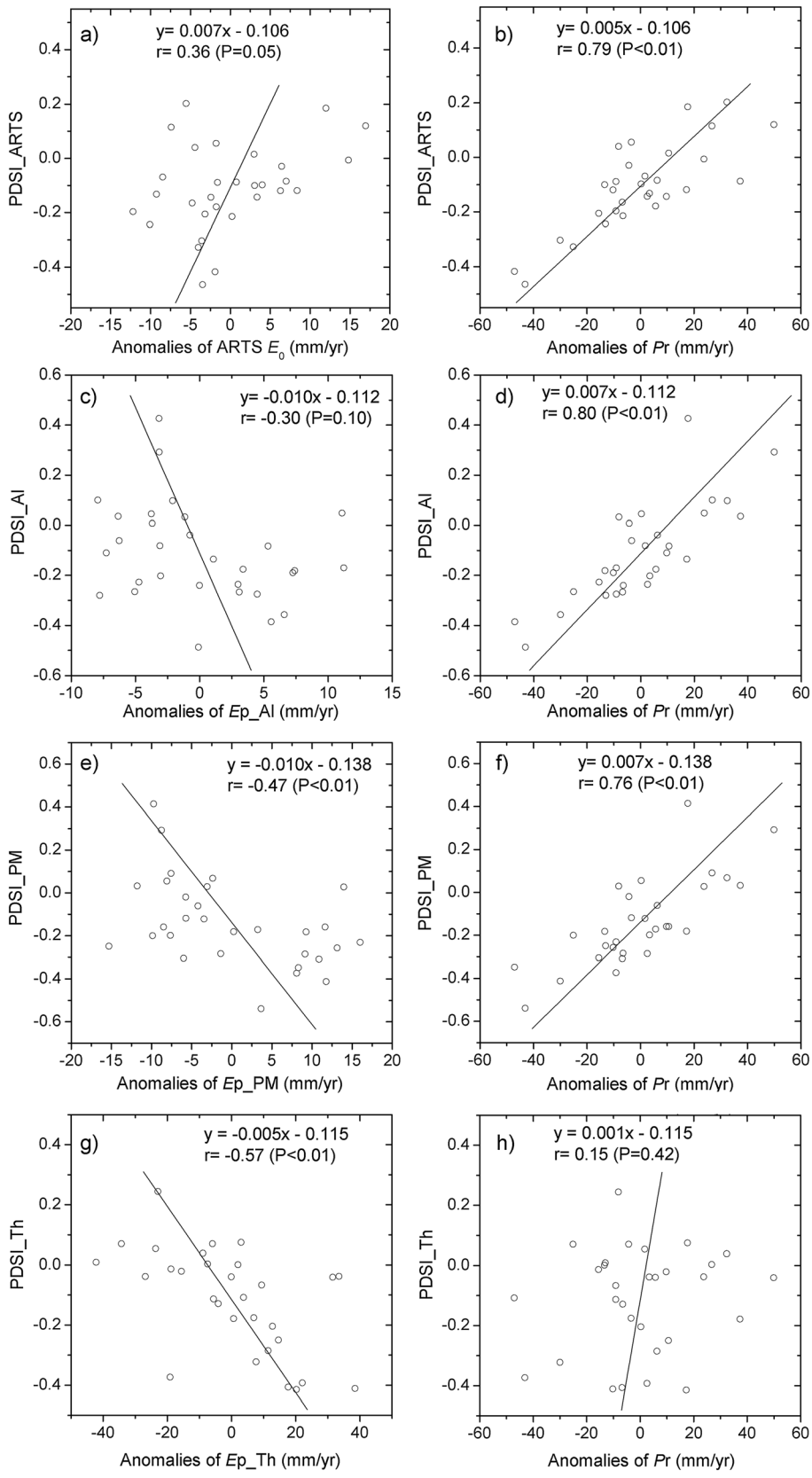

Figure 3. Scatterplots of annual anomalies of PDSI_ARTS, PDSI_AI, PDSI_PM, and PDSI_Th versus (a, c, e, and g) E_p (or E_0) and (b, d, f, and h) CRU P_r over 1982–2011.

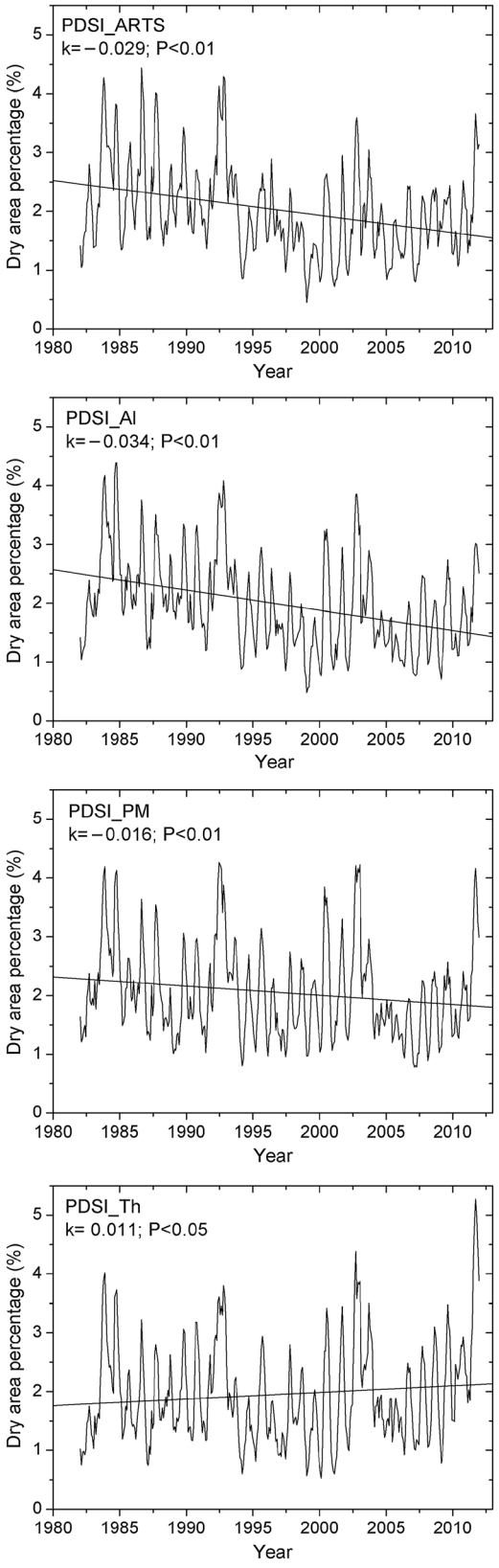

Figure 4. Time series of globally monthly dry area percentage with PDSI ≤ -4 derived from self-calibrating PDSI_ARTS, PDSI_AI, PDSI_PM, and PDSI_Th over 1982–2011.

system. What causes the opposite trends? It appears that the PDSI_Th gave a distinctive trend of drought primarily due to the different parameterization for E_P. Figure 2d shows that E_{P_Th} had the most significant increasing trend among four E_P models with an increase of 14.9 mm per 10 years—almost treble the increasing trend (i.e., 5.1 mm per 10 years) of ARTS E_0 (Figure 2a). However, both E_{P_AI} and E_{P_PM} had no significant change during past 30 years.

Drought in the PDSI model is mainly determined by two driving factors, precipitation (P_r) and E_P. One would expect their interannual variations should jointly affect the drought trend. Further comparison of PDSI, CUR P_r and E_P trends shows that PDSI_ARTS (Figure 2a) had an increasing trend, i.e., a wetting trend, mainly due to P_r trend (14.7 mm per 10 years) suppressing the trend of ARTS E_0 (5.1 mm per 10 years). Similarly, both Allen and PM PDSI had a wetting trend mainly resulting from the increasing water supply of P_r and stable E_P (Figures 2b and 2c). However, E_{P_Th} (Figure 2d) had an increasing trend of 14.9 mm per 10 year much higher than that of CUR P_r (14.7 mm per 10 years), which results in the drying trend shown by PDSI_Th. The patterns of precipitation and E_P determined the final drought or wet trend derived from the PDSI model (Figure 2). PDSI_ARTS and PDSI_Th had opposite trends (Figure 1) due to using respective ARTS E_0 and E_{P_Th} in the same scPDSI model. The scPDSI model is sensitive to the input E_P. This coincides with the *Sheffield et al.* [2012] finding that as a simplified E_P model, E_{P_Th} produces an overestimated increase of global drought. More controversial studies [*van der Schrier et al.*, 2011; *Dai*, 2011] show that PDSI values are insensitive to the parameterizations for E_P.

Further correlation analysis shows (Figure 3) large differences in correlation r between PDSI and its driving factors of P_r and E_P. Annual average of PDSI_ARTS, PDSI_AI, and PDSI_PM (Figures 3a, 3c, and 3e) all had a positive relationship ($P < 0.01$) with annual P_r with a correlation r over 0.76 indicating drought is mainly determined by P_r and below-normal P_r results in severe droughts. PDSI_AI and PDSI_PM (Figures 3d and 3f) had a negative relationship with E_{P_AI} and E_{P_PM}. Increasing E_P benefits the development of drought. In contrast, PDSI_ARTS had a positive relation with ARTS E_0 (Figure 3a), which differed from the negative relations observed among other E_P and corresponding PDSI (Figures 3d, 3f, and 3h). Because ARTS E_0 considers the impacts of

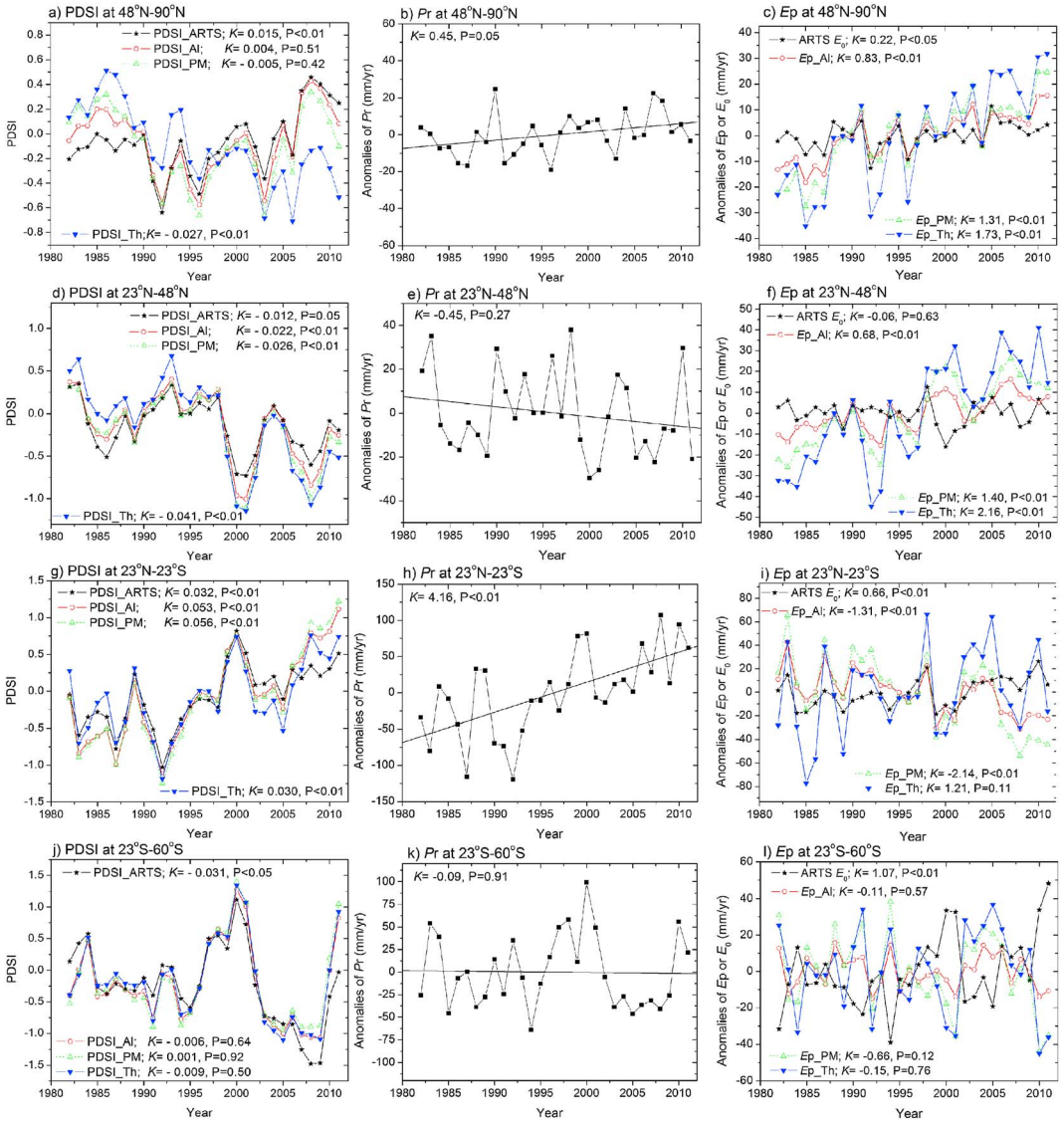

Figure 5. Time series of latitudinal averaged annual anomalies of (left) self-calibrating PDSI values, (middle) P_r, and (right) E_P (or E_0) at four latitude zones (i.e., 48°N–90°N, 23°N–48°N, 23°S–23°N, 48°S–60°S) over 1982–2011.

vegetation and relative humidity, the ARTS E_0 conceptually differs from traditional E_P calculations such as E_{P_PM}.

Figure 3h shows that PDSI_Th did not change with a decrease of P_r, but PDSI_Th (Figure 3g) had a negative correlation ($P < 0.01$) with E_{P_Th}. It can be concluded that it is E_{P_Th} not P_r that determines the development of drought shown by PDSI_Th. This obviously opposes the common knowledge that drought predominantly results from a deceasing P_r.

Figure 4 shows monthly variations of global dry area (in percentage) corresponding to extremely dry conditions with PDSI < -4 (Table 1). Dry area, derived from PDSI_ARTS, PDSI_AI, and PDSI_PM, significantly decreased (Figure 4), but dry area detected by PDSI_Th had an increased trend ($P < 0.05$) during past 30 years similar to the drying trend shown by PDSI_Th index (Figure 1a). The analysis above showed that PDSI_Th resulted in an opposite trend of dry area, mainly due to different E_P parameterization compared with PDSI_PM, PDSI_ARTS, and PDSI_AI, which agrees with the *Sheffield et al.* [2012] finding that there is a large difference in trend of dry area derived from PDSI_PM and PDSI_Th after 1980.

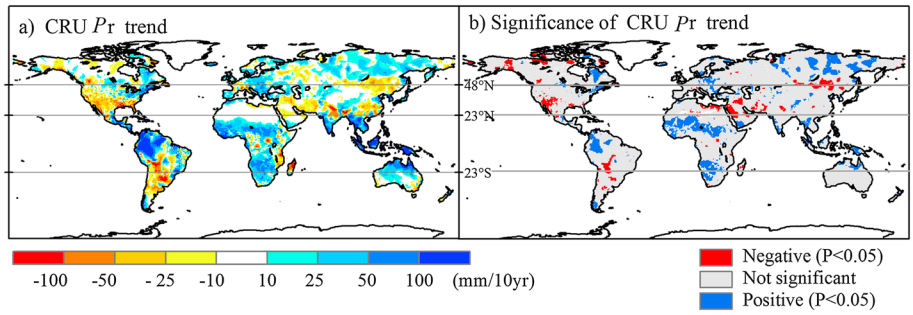

Figure 6. Trend map (a) of CRU P_r and (b) its significance over 1982–2011. Note that grey lines show the latitude of 48°N, 23°N, and 23°S, respectively.

4.2. Interannual Variations of Latitudinal PDSI, E_P, and P_r

Does PDSI show similar interannual variations at different latitudes? Figure 5 shows a large difference in interannual variations of PDSI at different latitudes. In high latitudes (48°N–90°N) of the Northern Hemisphere (Figures 5a–5c), P_r increased but had no significant trend ($P = 0.05$); only PDSI_Th had a drying trend of −0.27 per decade, i.e., drought mainly resulted from its driving factor E_{P_Th} that increased by 17.3 mm per

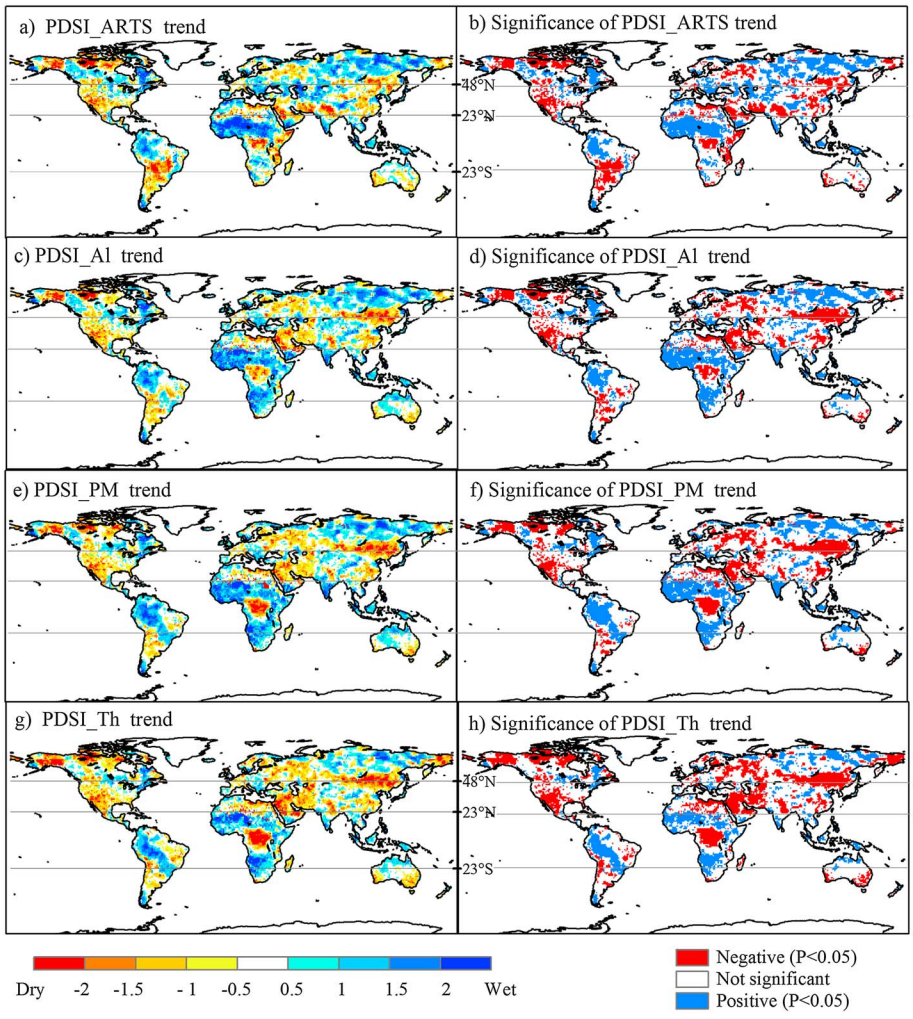

Figure 7. Trend maps of annual PDSI_ARTS, PDSI_Al, PDSI_PM, and PDSI_Th over 1982–2011 and their corresponding significance.

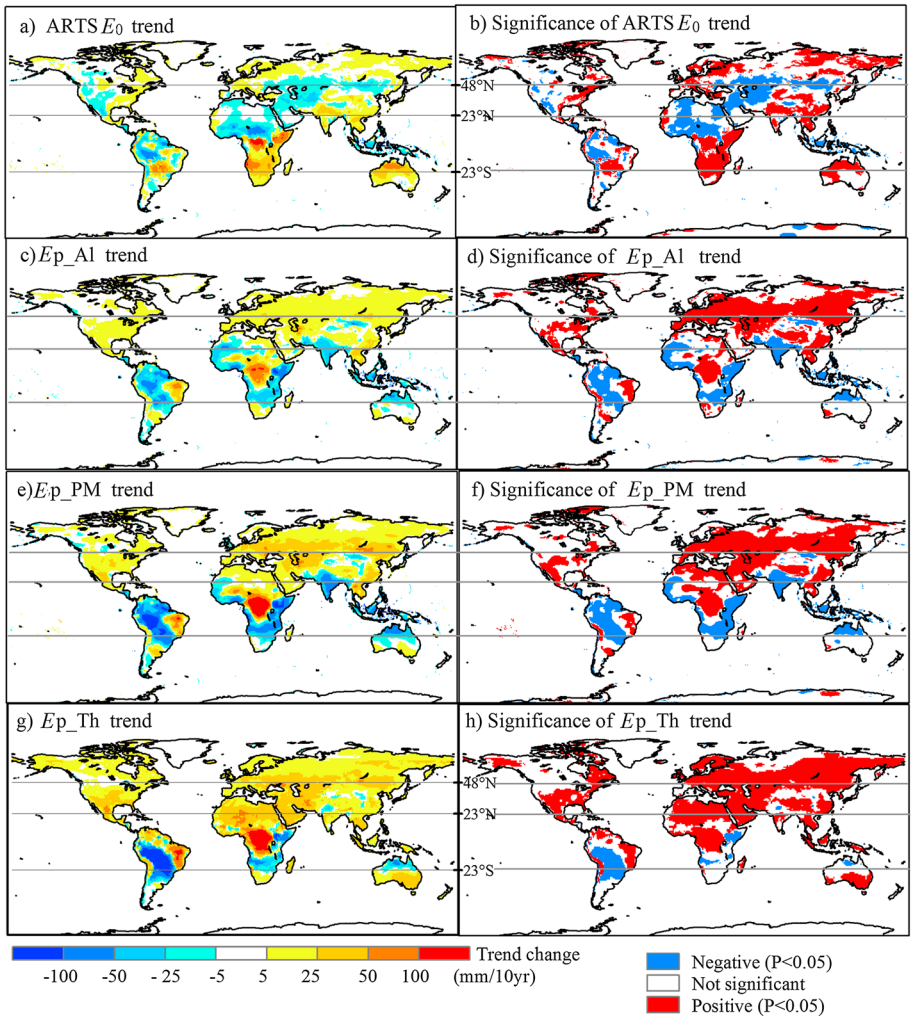

Figure 8. Trend maps of annual (a) ARTS E_0, (c) Allen E_P, (e) PM E_P, and (g) Thornthwaite E_P over 1982–2011 and (b, d, f, and h) their corresponding significance.

10 years. Although E_{P_Al} and E_{P_PM} had an increasing trend, their corresponding PDSI had no significant trend. In contrast, PDSI_ARTS showed a wetting trend of 0.15 per decade because ARTS E_0 had a weak increasing trend of 2.2 mm per 10 years.

In the midlatitudes (23°N–48°N) of the Northern Hemisphere (Figures 5d–5f), PDSI_ARTS and other three PDSIs all decrease with a decreasing P_r. However, the PDSI_ARTS had no significant trend due to weak variation of ARTS E_0 and P_r, while other three PDSIs show a drought trend because of significantly increasing E_{P_Al}, E_{P_PM}, and E_{P_Th}.

In the tropics (23°S–23°N), all PDSIs (Figures 5g–5i) showed a wet trend of over 0.3 per 10 years mainly because P_r increased by 41.6 mm per 10 years. However, ARTS E_0, E_{P_Al}, E_{P_PM}, and E_{P_Th} featured different variations; E_{P_Al} and E_{P_PM} decreased while ARTS E_0 and E_{P_Th} increased, but the variation of E_{P_Th} was not significant.

In middle to high latitudes (48°N–90°N) of the Southern Hemisphere, P_r (Figure 5k) had no significant trend of variation ($P = 0.91$); ARTS E_0 (Figure 5l) had an increasing trend of 10.7 mm per 10 years, and other three E_P models had no significant trend. As a result, only PDSI_ARTS (Figure 5j) showed a drought trend ($P < 0.05$) of 0.33 per 10 years while other three PDSIs had no significant trend.

In short, a large difference in latitude variations of the PDSI also resulted from the coupling effects of two driving factors of P_r and E_P. PDSI values are most sensitive to the parameterizations for E_P in high latitude (48°N–90°N) of the Northern Hemisphere (Figure 5a) because the most significant warming occurred in the

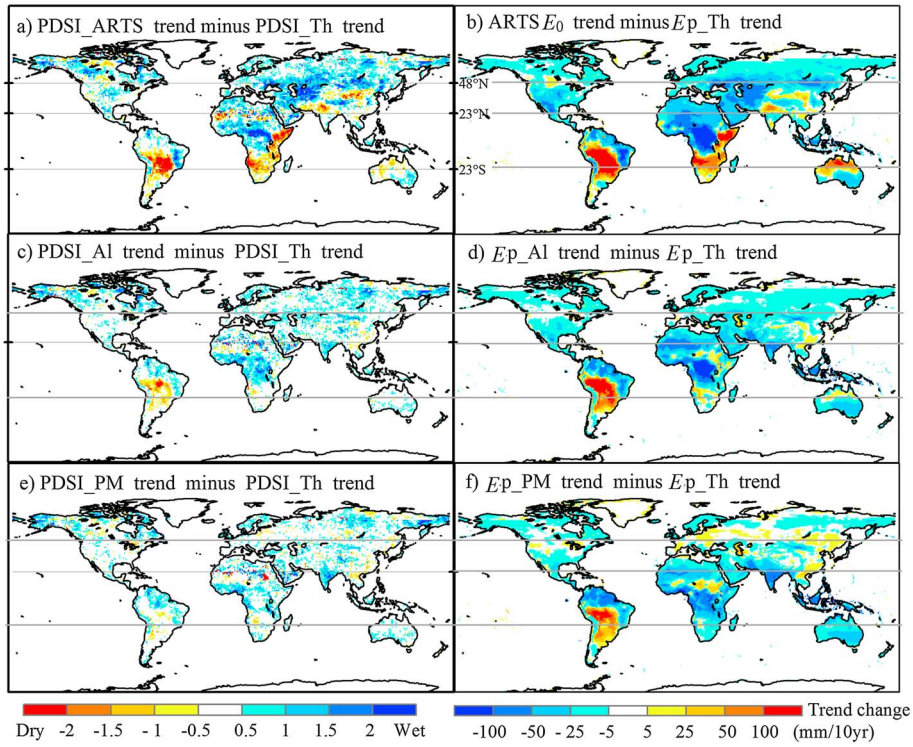

Figure 9. Trend differences of (a) PDSI_ARTS, (c) PDIS_Al, and (e) PDSI_PM minus PDSI_Th, respectively, and (b) ARTS E_0, (d) E_{P_Al}, and (f) E_{P_PM}, minus E_{P_Th}, respectively, over 1982–2011.

northern high latitude with a trend of MERRA $T = 0.43$°C per 10 years, which causes a higher E_{P_Th} and a drying trend as a result that contradicts the increasing P_r and the wetting trend denoted by PDSI_ARTS. In contrast, the other latitudinal zones are insensitive.

4.3. Spatial Variations of PDSI, E_P, and P_r

Figure 6 shows that high latitudes (48°–90°N) of the Northern Hemisphere featured more P_r especially in Russia and eastern Canada. Midlatitude (23°N–48°N) of the Northern Hemisphere experienced decreasing P_r. Most tropical regions were characterized with increasing P_r. With respect to middle to high latitudes (23°S–60°S) of the Southern Hemisphere, southern South America featured decreasing P_r while southern Africa featured increasing P_r. In short, four latitudinal belts featured different trends of P_r during the past 30 years. Then we might have a question whether P_r resulted in a similar spatial pattern of drying trend in corresponding latitudinal belts.

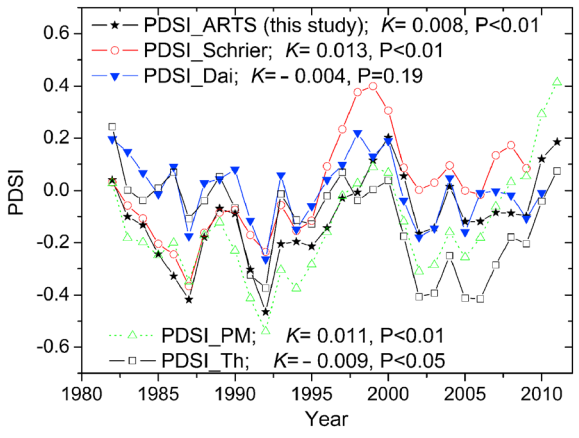

Figure 10. Time series of globally averaged annual anomalies of PDSI_ARTS, PDSI_PM, and PDSI_Th over 1982–2011, PDSI_Schrier over 1982–2009, and PDSI_Dai over 1982–2010, respectively.

Figure 7 shows that spatial variations of four PDSI trends had a similar pattern to that of P_r. Russia and eastern Canada in high latitudes (48°N–60°N) of the Northern Hemisphere feature a wetting trend due to more P_r. Midlatitudes (23°N–48°N) of the Northern Hemisphere experienced a drying trend corresponding to the decreasing P_r. Most tropical regions were characterized with a wetting trend related to the increasing P_r. With

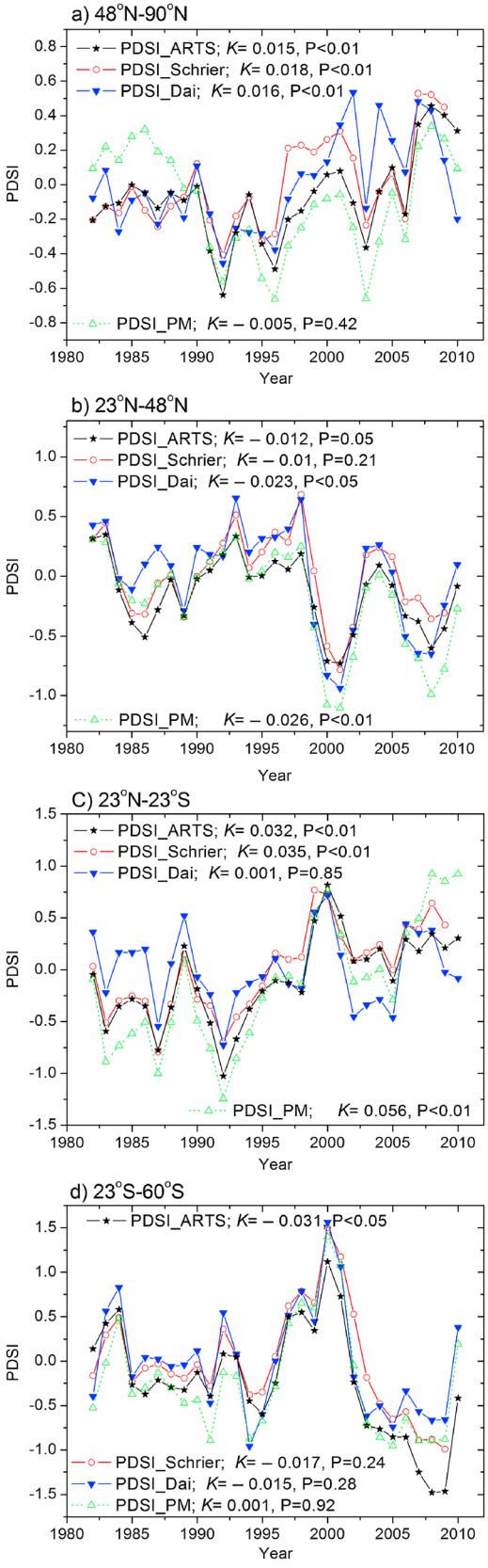

Figure 11. Time series of latitudinal averaged annual anomalies of PDSI_ARTS, PDSI_PM, PDSI_Schrier, and PDSI_Dai at four latitude zones of (a) 48°N–90°N, (b) 23°N–48°N, (c) 23°S–23°N, and (d) 48°S–60°S.

respect to middle to high latitudes (23°S–60°S) of the Southern Hemisphere, southern South America featured a drying trend following a decreasing P_r, while southern Africa featured a wetting trend accompanied by an increasing P_r. Thus, spatial variations of four PDSI trends over global land were similar and determined majorly by the pattern of P_r trend. However, the drying trend in some regions did not always relate with significant decreasing P_r. For example, there is no significant P_r trend in western Russia and central Africa, but a significant drying trend occurred in these regions. One might wonder whether E_P was responsible for the abnormal pattern of drying trend that cannot be explained by the P_r trend.

Figure 8 clearly shows that ARTS E_0 and other E_P models all had an increasing trend in western Russia and central Africa which resulted in the drying trend denoted by PDSI values in Figure 7. In contrast, E_{P_AI} and E_{P_PM} had a similar pattern of changing trend; they featured an increasing trend in most North America and Euro-Asia continents, but they showed a decreasing trend in tropical regions except the central Africa and eastern South America; they had no significant trend in the Southern Hemisphere (23°N–60°N). However, E_{P_Th} and ARTS E_0 differed from E_{P_AI} and E_{P_PM} in the spatial pattern of changing trend. For instance, E_{P_Th} had an opposite, increasing trend in India and tropical Asia. ARTS E_0 had an increasing trend in northern Australia, southern Africa, and India and decreasing trend in western North America and West Asia.

We also compared PDSI and E_P values of Thornthwaite with that of ARTS, Allen, and PM. Figure 9 shows that PDSI_Th often overestimated the drying trend. Locations where PDSI_Th overestimated the drying trend often corresponded to a positive difference between E_{P_Th} and other E_Ps (i.e., ARTS E_0, E_{P_AI}, E_{P_PM}), confirming the conclusion that PDSI trend is sensitive to the parameterization of E_P formula used in the PDSI model; the reverse is also true.

4.4. Comparison With Other PDSI Data Sets

Figure 10 shows comparison of PDSI_ARTS, PDSI_PM, and PDSI_Th with two published PDSI products. PDSI_Scheier [*van der Schrier et al.*, 2013] tends to increase by 0.13 per 10 years which is

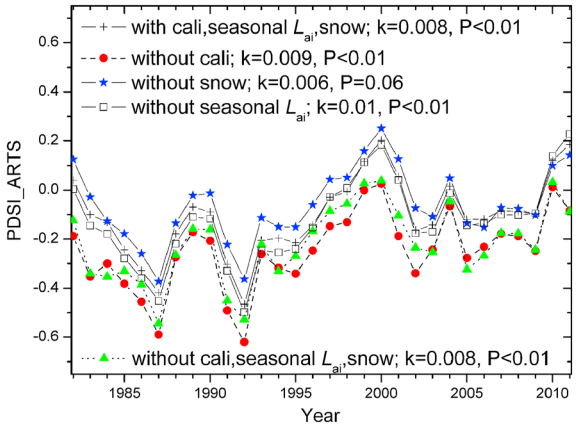

Figure 12. Globally averaged annual anomalies of PDSI_ARTS with or without automatic calibration (cali), seasonal vegetation LAI, and snowmelting (snow), respectively, over 1982–2011.

consistent with the increasing trend of PDSI_ARTS ($k = 0.08$ per 10 years) and PDSI_PM ($k = 0.11$ per 10 years); however, PDSI_Dai [*Dai*, 2011] has no significant change during past 29 years.

In addition, we analyzed trends of PDSI_Scheier and PDSI_Dai over four latitudinal regions. In high latitudes (48°N–90°N) of the Northern Hemisphere, both PDSI_Scheier and PDSI_Dai (Figure 11a) have an increasing trend of 0.18 and 0.16 per 10 years, respectively, which confirms the wet trend of 0.15 per 10 years given by PDSI_ARTS. In midlatitudes (23°N–48°N) of the Northern Hemisphere, (Figure 11b) PDSI_Dai indicates a drought trend of –0.23 per decade similar to PDSI_PM; however, PDSI_Scheier has no significant trend similar to PDSI_ARTS. In tropical regions (23°S–23°N), PDSI_Scheier (Figure 11c) shows a wetting trend ($P < 0.01$) with slope $k = 0.35$ per 10 years, similar to PDSI_ARTS and PDSI_PM; however, PDSI_Dai has no significant trend. In middle to high latitudes (23°S–60°S) of the Southern Hemisphere, both PDSI_Scheier and PDSI_Dai (Figure 11d) have no significant trend like PDSI_PM; however, PDSI_ ARTS shows a drought trend of 0.33 per decade. In short, PDSI_ ARTS had a similar performance to PDSI_Scheier in drought monitoring, but large differences were observed between PDSI_Dai and PDSI_Scheier, which is attributed to the selection of a calibration period that amplifies the dry trend by *van der Schrier et al.* [2013]. However, we found the different precipitation data resulted in the difference of PDSI trend because CRU P_r ingested by PDSI_ARTS had a higher increasing trend of 1.53 mm yr^{-1} ($P < 0.01$) than that of 0.34 mm yr^{-1} ($P = 0.37$) for Global Precipitation Climatology Project (GPCP) P_r over 1982–2011 [*Yan et al.*, 2013]. As CRU gauge-based P_r had a better response to recent La Niña events compared with GPCP satellite-based P_r, thus the global wetting trend given in this study is reasonable.

4.5. Sensitivity of PDSI_ARTS to the Model Parameterization and Input Data

To investigate the impact due to the use of seasonal vegetation, snowmelting, and automatic calibration in the fame of ARTS PDSI model, we calculated PDSI_ARTS with or without automatic calibration, seasonal vegetation LAI, and snowmelting, respectively, over 1982–2011. Figure 12 shows that all PDSI_ARTS had an increasing tendency (i.e., a wetting trend) except snowmelting-excluded PDSI_ARTS. Regardless of snowmelting process, the self-calibrating PDSI_ARTS had no significant trend ($P = 0.06$). Conversely, the use of snowmelting module contributed to the wetting trend ($P < 0.01$) of PDSI_ARTS during the research period (Figure 12), which is consistent with the findings of *Barichivich et al.* [2014] that the water supplied by the spring melting of the winter snowpack plays a dominant role in summer wetting as well as the enhanced vegetation activity at northern latitudes (>45°N). Hence, snowmelting process should be included in the PDSI model.

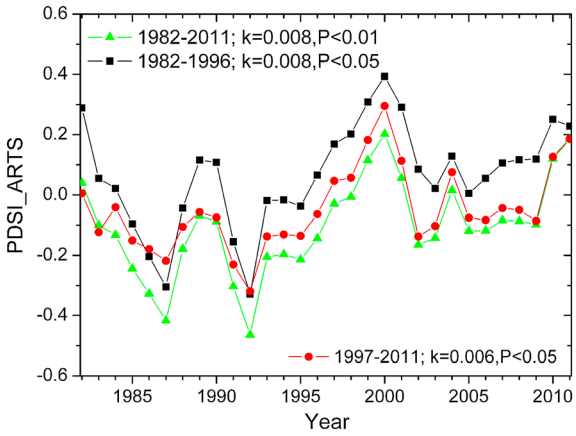

Figure 13. Globally averaged annual anomalies of PDSI_ARTS over 1982–2011 but with different calibration period, i.e., entire period (1982–2011), first 15 years (1982–1996), and last 15 years (1997–2011).

The use of original PDSI instead of the self-calibrating PDSI also gave an increasing trend ($P < 0.01$) of PDSI_ARTS. However, original PDSI_ARTS had a damped variability as shown

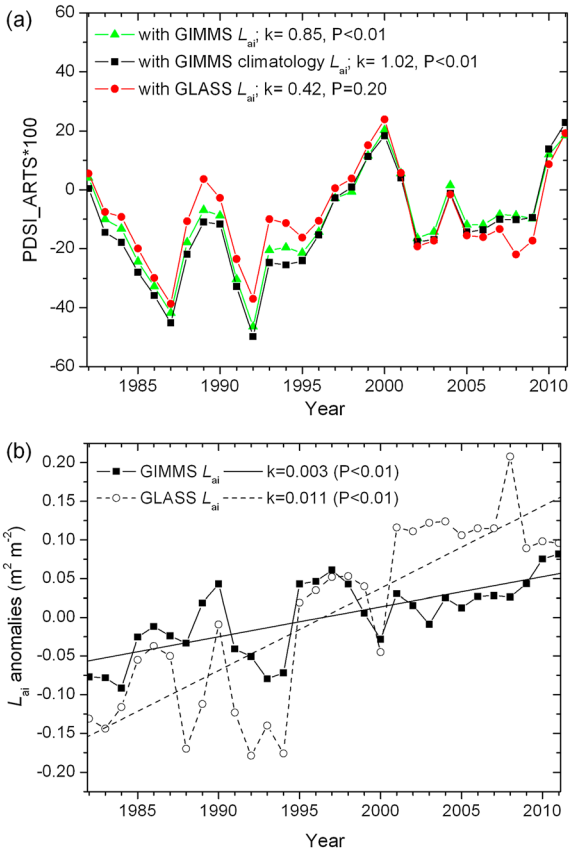

Figure 14. Globally averaged annual anomalies of (a) self-calibrating PDSI_ARTS driven with GIMMS LAI, GIMMS climatology LAI, and GLASS LAI, respectively, and (b) GIMMS and GLASS LAI over 1982–2011.

by *Sheffield et al.* [2012] and a much lower value compared with self-calibrating PDSI_ARTS. In addition, to investigate the impact of the selection of calibration period on self-calibrating PDSI, we designed an experiment with calibration period defined as entire period (1982–2011), first 15 years (1982–1996), and last 15 years (1997–2011), respectively. Figure 13 shows that PDSI_ARTS calibrated over different periods all increased but with different significance; i.e., entire period (1982–2011) as the calibration period featured a higher significance ($P < 0.01$) than that ($P < 0.05$) of other two calibration periods. In short, the selection of calibration period did not significantly affect the PDSI results in this study, which differs from the conclusion of *van der Schrier et al.* [2013] that the selection of calibration period obviously affected the trend of self-calibrating PDSI, and it is the principal reason for the disparate results of recent global drying or not.

To understand the sensitivity of PDSI_ARTS to vegetation index, we conducted the PDSI_ARTS simulation with the GIMMS climatology mean LAI instead of the GIMMS historical one, which (Figure 14a) shows that the PDSI_ARTS with GIMMS climatology LAI also had an increasing trend ($P < 0.01$), i.e., a wetting trend, similar to PDSI_ARTS driven with GIMMS historical LAI.

We further simulated the drought trend using GLASS historical LAI instead of the GIMMS historical LAI, which (Figure 14a) shows that PDSI_ARTS driven with GLASS LAI had no significant trend ($P = 0.20$). The different drought trend was due to using different long-term LAI time series, i.e., GIMMS LAI and GLASS LAI. Figure 14b shows that GLASS LAI increased with a slope of $k = 0.011$ significantly higher than that ($k = 0.003$) of GIMMS LAI, which resulted in an increasing GLASS LAI-based ARTS E_0 with a higher trend than that of GIMMS LAI-based ARTS E_0 and in turn the nonsignificant change of PDSI_ARTS. It can be concluded that PDSI_ARTS model was also sensitive to input data of LAI, which has rarely been addressed in previous studies.

As the estimated wetting trend is an outcome of input data sets and model, we evaluated the MERRA *T* with CRUTEM4 *T* [*Jones et al.*, 2012; *Osborn and Jones*, 2014] that has been used by Intergovernmental Panel on Climate Change climate report (CRUTEM4 *T* data was downloaded at http://www.metoffice.gov.uk/hadobs/crutem4/data/download.html). Figure 15a shows that CRUTEM4 *T* had an increasing trend of 0.87°C 30 yr^{-1} which is higher than the trend of 0.72°C 30 yr^{-1} for MERRA *T*. Further simulations of PDSI_ARTS driven with CRUTEM4 *T* instead of MERRA *T* (Figure 15b) show that CRUTEM4 *T*-based PDSI_ARTS also increased ($P < 0.01$) indicating a wetting trend similar to PDSI_ARTS driven with MERRA *T*, which agrees well with the conclusion that global warming may not cause droughts [*Trenberth et al.*, 2014]. In short, MERRA *T* had a similar potential to CRUTEM4 *T* in driving PDSI_ARTS model to study the drying trend.

5. Discussion

The sensitivity of PDSI values to the parameterizations for E_P is a topic of ongoing argument. *Dai* [2011] and *van der Schrier et al.* [2011] found that the choice of the E_{P_Th} and E_{P_PM} had small effects on the global drying trend and their PDSI values were similar in terms of statistics and drying area. *van der Schrier et al.*

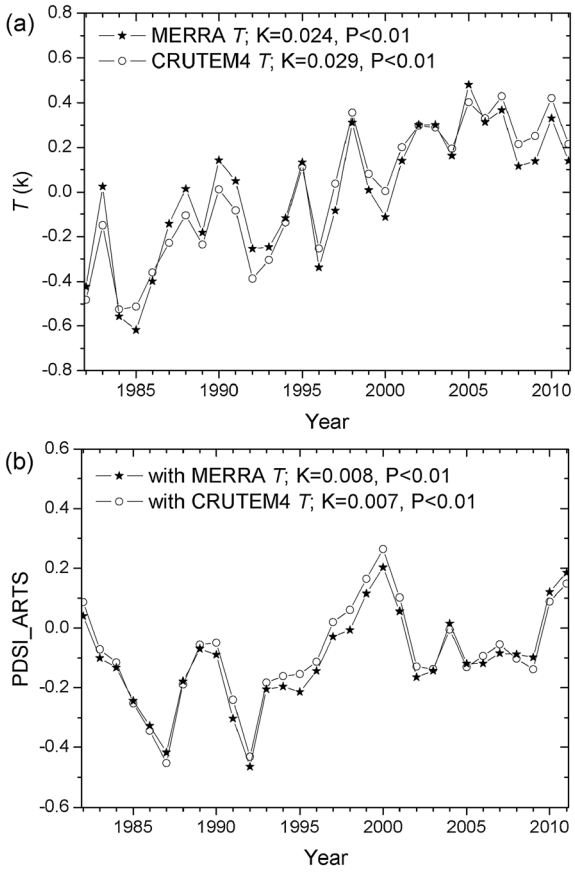

Figure 15. Globally averaged annual anomalies of (a) MERRA *T* and CRUTEM4 *T* and (b) corresponding self-calibrating PDSI_ARTS over 1982–2011.

[2013] and *Dai* [2011] attributed this insensitivity to the calculations in the simple water balance model because actual evaporation, often limited by the available moisture on the ground, affects the water balance.

However, our study and *Sheffield et al.* [2012] found that PDSI values are sensitive to the choice of the E_{P_Th} and E_{P_PM}; the use of E_{P_Th} in the PDSI model produces an overestimated increase of global drought. *Hobbins et al.* [2008] and *Sheffield et al.* [2012] pointed out that the choice of parameterization for E_P is critical in energy-limited regions such as the Amazon and northern Eurasia because E_P determines the final actual evaporation and soil moisture, and E_{P_Th} often leads to errors in energy-limited regions. This study found that in high latitude (48°N–90°N) of the Northern Hemisphere (an energy-limited region), PDSI_Th showed a drying trend different from that of PDSI_PM because E_{P_Th} had a higher uptrend than that of E_{P_PM} (Figure 2). This, in turn, contributed to global drying trend denoted by global PDSI_Th over the past 30 years. While seldom addressed in previous studies, the choice of E_{P_Th} results in the decrease of PDSI value in high latitude of the Northern Hemisphere and even affected the sign of the global PDSI trend. One should be cautious when E_{P_Th} is applied to global drought research.

Since E_P plays a key role in the forming of drought besides precipitation, more realistic E_P models have been adopted to drive the PDSI model, which improves our knowledge of drought related with global temperature rising. Use of a more physiological E_{P_PM} model, which takes into account more factors of available energy, humidity, and wind speed, found little change in drought from 1950 to 2008 [*Sheffield et al.*, 2012]. This corrects the previous finding that drought tends to become more severe and more widespread since the 1950s as a result of global warming [*Dai*, 2011]. This arises from the use of a simple E_{P_Th} model that only takes into account temperature and latitude. A more recent PDSI, derived from E_{P_PM} using the actual vegetation cover rather than a reference crop, also does not support the global strong drying pattern for the 1950–2009 period [*van der Schrier et al.*, 2013].

However, there remains the issue of seasonal vegetation changes, which is absent in previous E_P and PDSI models. This absence has been criticized as unrealistic in E_P models [*Alley*, 1984]. In our study, ARTS_PDSI initially considers the interannual and seasonal changes of vegetation LAI by using a canopy conductance model, which reveals global wetting during the past 30 years of 1982–2011. Similarly, *van der Schrier et al.* [2013] reported a decrease of drying from the mid-1980s onward. Thus, PDSI_ARTS can be applied to global drought study due to more physical processes included while PDSI_PM or PDSI_AI can be used alternatively in case of no LAI data.

It is widely accepted that drought is often caused by below-normal precipitation and PDSI model deduces the drought from the interactive effect of P_r and E_p. Numerous PDSI-based drought studies [*van der Schrier et al.*, 2013; *Sheffield et al.*, 2012; *Dai*, 2011] have focused attention to the E_P variations irrespective of precipitation variations that is also associated with global warming.

Numerous precipitation and runoff observation and numerical experiments confirm an ongoing intensification of global hydrologic cycle with global temperature increase following the Clausius-Clapeyron law [*Huntington*, 2006; *Wentz et al.*, 2007; *Gerten et al.*, 2008; *Alkama et al.*, 2011]. For instance, global land P_r had an uptrend of 2.5% over 1901–2002 based on CRU TS2.1 climatology [*Gerten et al.*, 2008]. Similarly, we found an uptrend of 3.1% for global land P_r over 1982–2011 based on the latest CRU P_r data set accompanied by an unusual global warming [*Allan et al.*, 2010; *Liu and Allan*, 2013].

Thus, it is reasonable that the global land became wetter during past 30 years, as deduced from PDSI_ARTS, PDSI_PM, and PDSI_AI in this study. This bridges the gap between the global drought status and the intensified hydrological cycle from global warming. Significantly, different latitudinal zones had different responses to global warming and precipitation variation, i.e., tropical and high latitude (48°N–90°N) of the Northern Hemisphere became wetter due to increased precipitation while midlatitude (32°N–48°N) of the Northern Hemisphere became drier due to decreased precipitation, which is rarely addressed in past researches.

Contrary to common knowledge that drought is often caused by below-normal precipitation, we further found that PDSI_Th had a significant negative relationship with interannual variation of E_{P_Th} but no significant relation with P_r. PDSI_ARTS, PDSI_AI, and PDSI_PM all were sensitive to interannual variation of P_r rather than E_P or E_0 and P_r still played a determining role in the development of drought during past 30 years. Although global average temperature has increased, global warming and its related-E_P variation do not change the causal relationship between P_r and drought up to the present.

Why does global drought have obvious interannual variations shown in Figure 1? The source is the El Niño–Southern Oscillation (ENSO), the most prominent ocean-atmosphere phenomenon resulting in large-scale climate (rainfall, drought, temperature, evapotranspiration, etc.) variability on interannual time scales [*Dai et al.*, 1997; *Wolter and Timlin*, 1998; *Bonsal and Lawford*, 1999; *Vicente-Serrano et al.*, 2011; *Miralles et al.*, 2014; *Yan et al.*, 2013]. Warm ENSO events (El Niño) tend to decrease global land precipitation and cold ENSO events (La Niña) tend to increase global land precipitation [*Gu et al.*, 2007]. Accordingly, El Niño events tend to cause more global drought than La Niña events [*Sheffield et al.*, 2009; *Vicente-Serrano et al.*, 2011]. With regard to this study, CRU P_r and PDSI_ARTS had significant increases from 1982 to 2011. This agrees well with ENSO variations such that El Niño impact was weakening, while La Niña impact was intensifying with more land P_r than normal during the 30 years [*Yan et al.*, 2013].

In summary, ENSO affects the global drought variation mainly via global precipitation anomalies. As El Niño and La Niña events alternates with each other in ENSO history [*Wolter and Timlin*, 2011], it is expected that dry spells alternates with wet spells, which confirms the findings of *Sheffield et al.* [2012] and *van der Schrier et al.* [2013] that there is no strong signal for global drying or wetting for a long period of past 60 years from 1950 to 2008. However, during a short period such as 30 years in this study, ENSO as well as increased P_r leads to global wetting.

Recent 2009–2011 ENSO cycle also demonstrated a transition from 2009–2010 El Niño phase to 2010–2011 La Niña phase that even resulted in a 5 mm drop in global sea level as excess precipitation deposited water on land [*Boening et al.*, 2012]. Thus, when year 2010–2011 representing an extreme wet condition was disregarded, we can find little change in global drought shown by PDSI_ARTS or PDSI_PM from 1982 to 2009 (not shown) compared with the wetting trend ($P < 0.01$) from 1982 to 2011, which shows that during a short period of 30 years, ENSO-related precipitation variation might significantly affect drying trend and even conceal the impact of global warming. Similarly, *Trenberth et al.* [2014] pointed out that accurate understanding of drought requires an improvement in the precipitation driving data as well as the accounting for natural variability, especially ENSO effects because of preference for wetter land during La Niña events.

However, recent studies reported drying trend. For instance, remotely sensed soil moisture showed drying soil moisture from 1998 to 2008 [*Jung et al.*, 2010], which is due to 1999/2000 representing the strongest La Niña event in the research period of 1998 to 2008 leading to a summit of precipitation, and thereafter the precipitation decreased and soil became drier until 2008. This short-term drying trend over 11 years was also observed by PDSI_ARTS in this study. *Zhou et al.* [2014] found a widespread decline of Congo rainforest greenness in the past decade indicating a drying trend, which was also captured in Congo rainforest of western tropical Africa (Figure 7) by ARTS_PDSI over 1982–2011. In short, these direct evidence

Table 2. Annual Mean of Four Types' Potential Evaporation (E_P) and Associated Actual Evapotranspiration (E) for Global Land Excluding Antarctica and Greenland[a]

Type	ARTS	Allen	Penman	Thornthwaite
E_P	80.5	119.5	156.5	127.3
E	66.4	72.7	79.3	73.1

[a]Unit: 10^3 km^3 yr^{-1}.

of drying trend mainly occurred either in regional scale or over a short period of 11 years, which does not contradict the wetting trend over 1982–2011 given by PDSI_ARTS.

Comparison of averaged values of E_P (i.e., ARTS E_0, E_{P_AI}, E_{P_PM}) shows a large difference; E_{P_PM} is almost 2 times the ARTS E_0 (Table 2). But their corresponding PDSI values had minor differences (Figure 1); i.e., PDSI model is insensitive to absolute value of E_P because PDSI is finally determined by the ratio of actual values to potential values (i.e., $\alpha_i = \overline{E}_i/\overline{Ep}_i$) for evapotranspiration, recharge to soil layers, runoff, and water loss in scPDSI model (see equation (A1)). In concept, *Palmer* [1965] assumed that PDSI model will produce actual values such as actual E by using soil water balance model with input of E_P and P_r. Rather, our results indicate that the so-called E value, derived from traditional E_P (i.e., E_{P_AI}, E_{P_PM}, E_{P_Th}), is not actual E (Table 2) and it is often higher than recent estimates of global $E = 65 \times 10^3$ km^3 yr^{-1} [*Jung et al.*, 2010; *Yan et al.*, 2013] because E_P does not include the effect of vegetation transpiration and the simple SWB module in PDSI model only considers the impact of soil water stress. However, ARTS E_0, as a two-source model, calculates plant transpiration separately via canopy conductance accounting for effects of vegetation dynamic and relative humidity, which produces the actual E with SWB model playing a role of soil water stress. In this sense, seasonal vegetation-based ARTS PDSI model partly realize the expectation of *Palmer* [1965].

The ARTS PDSI model takes into account issues of seasonal vegetation, snowmelting, and automatic calibration. Nonetheless, some important processes such as catchment hydrology should be, but are still not included, because catchment hydrology needs calibration with observed runoff data on fine temporal scales such as the daily scale. Thus, the ARTS PDSI model is primarily applied to global scale on monthly scales with available input data.

Some uncertainties still exist. Recent observation and model simulations indicate that precipitation become more intense but less frequent and light rain become more scarce due to global warming and air pollution [*Chou et al.*, 2011; *Shiu et al.*, 2012; *Qian et al.*, 2009] implying greater risk of flash floods as well as droughts [*Shiu et al.*, 2012]. This issue has not been solved for PDSI-type models on monthly scales. As PDSI models are sensitive to E_P parameterization and P_r data have a larger uncertainty than that of temperature T, it is better to compare other E_P parameterizations and P_r data sets in PDSI model to reduce uncertainties in the research of global drought. Similarly, *Trenberth et al.* [2014] concluded that discrepancies of drought monitoring arise not only from the PDSI formulation but also from the highly uncertain forcing data. Thus, further ensemble analysis of more E_P models and forcing data including precipitation will be conducted in next step of our work.

6. Conclusions

The interannual variations of PDSI_ARTS, PDSI_AI, and PDSI_PM indicate that global land, particularly in tropical regions, had become wetter rather than drier primarily due to increased precipitation over past 30 years. It is too early to make a prediction of global drying in the future without taking the effects of precipitation and ENSO into consideration.

PDSI values are sensitive to the parameterizations for E_p. Significantly increased E_{P_Th} even caused an overestimated drought by suppressing the wetting effect of increased precipitation on global scale and especially in high latitude of Northern Hemisphere compared with E_{P_AI}, E_{P_PM}, and ARTS E_0 over the past 30 years. Thus, with regard to global drought monitoring, ARTS E_0, E_{P_AI}, and E_{P_PM} are preferred to E_{P_Th}.

Different latitude zones feature different drying or wetting trends in response to climate change during the past 30 years. In high latitude (48°N–90°N) of the Northern Hemisphere, PDSI_Th had a drying trend but not supported by PDSI_ARTS, PDSI_AI, and PDSI_PM. However, in midlatitude (23°N–48°N) of the Northern Hemisphere, all PDSI decreased except PDSI_ARTS having no significant trend. Tropical zones had a wetting trend. In middle to high latitudes (23°S–60°S) of the Southern Hemisphere, PDSI_ARTS showed a drying trend while other PDSI values had no significant trend.

ARTS E_0 had a similar performance to E_{P_AI} and E_{P_PM} in monitoring global as well as tropical drought during past 30 years; however, differences still existed in other latitudinal zones. In concept, ARTS E_0 has considered the effect of seasonal vegetation and atmosphere humidity on canopy conductance, which differs from E_{P_AI} and E_{P_PM} in that these traditional E_P just representing the atmosphere evaporation demand. Application of ARTS E_0 prior to other E_P in drought monitoring coupled with PDSI model will highlight the effects of vegetation and relative humidity besides the effects of precipitation and E_p.

Appendix A: Calculation of Self-Calibrating PDSI Model

As original Palmer PDSI model (1965) uses weighting and duration factors derived from empirical calibration against a limited amount of data observed over the U.S. Great Plains, it has been criticized for its disability of comparison between divers climatological regions [*Wells et al.*, 2004]. To solve this drawback, the self-calibrating PDSI (scPDSI) [*Wells et al.*, 2004] model was developed within the frame of Palmer PDSI model (1965) and regarded as more appropriate for global drought monitoring [*Dai*, 2011; *van der Schrier et al.*, 2011]. The Palmer PDSI model and its revision of scPDSI model are briefly introduced in the following.

The Palmer PDSI model (1965) computes four values related to the soil moisture on monthly scale by using a two-layer soil water balance model [*Thornthwaite*, 1948] driven by precipitation (P_r) and potential evapotranspiraiton (E_p). The four values are evapotranspiraiton (E), recharge to soil layers (R), runoff (O), and water loss from soil layers (L). Based on E_P and the maximum soil available water content (M_{awc}) of the soil, Palmer PDSI model (1965) derives three potential values, e.g., potential recharge (R_p), potential runoff (O_p), and potential water loss (L_p). In addition, four water balance coefficients are calculated using local climate for each month *i:*

$$\alpha_i = \frac{\overline{E}_i}{\overline{E\mathrm{p}}_i} \quad \beta_i = \frac{\overline{R}_i}{\overline{R\mathrm{p}}_i} \quad \gamma_i = \frac{\overline{O}_i}{\overline{O\mathrm{p}}_i} \quad \delta_i = \frac{\overline{L}_i}{\overline{L\mathrm{p}}_i} \tag{A1}$$

where the overbar indicates an average value over a climate period. Then climatically appropriate for existing conditions (CAFEC) values can be obtained by multiplying four potential values with their water balance coefficients, e.g., $\delta_i L\mathrm{p}$ for CAFEC water loss. Four CAFEC values are combined to give the CAFEC precipitation, $\hat{P}_r$, which represents the required amount of precipitation to maintain a normal soil moisture level for a given month:

$$\hat{P}_r = \alpha_i E\mathrm{p} + \beta_i R\mathrm{p} + \gamma_i O\mathrm{p} - \delta_i L\mathrm{p} \tag{A2}$$

The difference $\left(D = P_r - \hat{P}_r\right)$ between the actual precipitation P_r and the CAFEC precipitation $\hat{P}_r$ represents the moisture departure, i.e., the excess or shortage of precipitation in a month. As D is not a normalized value and the same D have different meanings at different locations and different times, D cannot directly applied for drought monitoring. To solve this problem, Palmer PDSI model adopts a new weighting coefficient of K, approximating the climate characteristic of a location, to correct the D with their product defined as the moisture anomaly index $Z(Z = D \times K)$. The Z index is further used to compute the PDSI value for a given month *i:*

$$X_i = p \times X_{i-1} + q \times Z_i \tag{A3}$$

where X_{i-1} is the PDSI for the previous month and p and q are two coefficients called duration factors, which affect the sensitivity of PDSI to monthly moisture anomaly Z and previous month's PDSI. Originally, *Palmer* [1965] derived the values of $p = 0.897$ and $q = 1/3$ empirically from the linear slope analysis between the length and severity of the extreme droughts at two locations. To solve the shortcomings of empirical coefficients, the scPDSI model adopts a new method to automatically calculate the climatic characteristic K and duration factors (p and q) using local climate data, so that the scPDSI can be compared over different locations and different times [*Wells et al.*, 2004]. It can be found that P_r and E_P as key input data determine the final PDSI value through their interaction within the soil water balance model. Further detailed description of scPDSI model can be found in the reference [*Wells et al.*, 2004]. Note that P_r is replaced with water supply P defined as the sum of rainfall and snowmelt derived from a simple snowmelting module (see equation (8)) in this study.

Appendix B: Calculation of Potential Evapotranspiration Models

A brief summary of temperature-based and net radiation-based E_P models, used in this study, is given below.

1. *Thornthwaite* E_{P_Th} Model
   Palmer [1965] originally adopted the *Thornthwaite* [1948] E_P equation with input of monthly mean air temperature, latitude, and month. This study used the modified *Thornthwaite* E_P equation (E_{P_Th}, in mm d^{-1}) currently implemented in the National Climatic Data Center [*Karl*, 1986]:

$$E_{P\_Th} = \begin{cases} 0 & \text{if } T \le 0°C \\ 25.4 d_u \exp[-3.8633 + 1.7156B - B\ln(H) - B_u \ln(T)] & \text{if } 0 < T < 26.7°C \\ 25.4 d_u [\sin(T/57.3 - 0.166) - 0.76] & \text{if } T \ge 26.7°C \end{cases} \quad \text{(B1)}$$

$$H = \sum_{m=1}^{12} \left(\frac{\max(T, 0)}{5} \right)^{1.514} \quad \text{(B2)}$$

$$B = 0.492 + 1.79 \times 10^{-2} H - 7.71 \times 10^{-5} H^2 + 6.75 \times 10^{-7} H^3 \quad \text{(B3)}$$

$$d_u = \begin{cases} (d_0 + 0.0157)/1.57 & \text{if } d_0 \ge 0 \\ (3.141593 + d_0 + 0.0157)/1.57 & \text{if } d_0 < 0 \end{cases} \quad \text{(B4)}$$

$$d_0 = \tan^{-1} \left(\frac{\sqrt{\max\left(0.1, 1 - [\varphi(m)\tan(\theta)]^2\right)}}{-\varphi(m)\tan(\theta)} \right) \quad \text{(B5)}$$

   where T is monthly mean air temperature (°C) at 2 m height, $\varphi(m)$ is a month (m)-dependent coefficient, θ is the latitude, and B and H are two heat factors.
2. *Penman-Monteith* E_{P_PM} Model
   Monteith [1965] presented the widely cited approach for modeling potential and actual evapotranspiration, which combines the radiative and aerodynamic processes. When stomatal conductance is assumed to be zero, the E_{P_PM} equation can be derived [*Shuttleworth*, 1993]:

$$E_{P\_PM} = \frac{\Delta R_n + 6.43(1 + 0.536u)D}{\Delta + \gamma} \quad \text{(B6)}$$

   where E_{P_PM} is potential evapotranspiration (mm d^{-1}), R_n is net radiation, Δ is the gradient of the saturated vapor pressure to the air temperature (kPa), γ is the psychrometric constant, D is the vapor pressure deficit, and u is the wind speed (m s^{-1}) at 2 m height.
3. Allen Reference E_{P_AI} Model
   Allen et al. [1994] derived the Food and Agriculture Organization reference evapotranspiration model from the *Penman-Monteith* E_P model [1965]:

$$E_{P\_AI} = \frac{0.408\Delta(R_n - G) + \gamma \frac{900}{T+273} uD}{\Delta + \gamma(1 + 0.34u)} \quad \text{(B7)}$$

   where E_{P_AI} is reference evapotranspiration (mm d^{-1}), R_n is net radiation (MJ m^{-2} d^{-1}), and T is the air temperature (°C).

Acknowledgments
We acknowledge the use of the MERRA reanalysis data available at the Modeling and Assimilation Data and Information Services Center (MDISC) managed by the NASA Goddard Earth Sciences (GES) Data and Information Services Center (DISC), the CRU data of the British Atmospheric Data Centre (BADC), the global LAI3g and FPAR3g data sets available at Department of Earth and Environment of Boston University, GLASS LAI data from the Center for Global Change Data Processing and Analysis of Beijing Normal University, and the ISLSCP II global gridded soil data at Oak Ridge National Laboratory Distributed Active Archive Center (ORNL DAAC). This work was supported by National Natural Science Foundation of China (41171284 and 40801129), National Basic Research Program of China (2013CB430205), Chinese Academy of Sciences (XDA05050602-1), and partly funded by grants from a University of Virginia's Programs of Distinction grant to H.H. Shugart. The reviewers are thanked for their constructive remarks and suggestions.

References

Alkama, R., B. Decharme, H. Douville, and A. Ribes (2011), Trends in global and basin-scale runoff over the late twentieth century: Methodological issues and sources of uncertainty, *J. Clim.*, *24*(12), 3000–3014, doi:10.1175/2010JCLI3921.1.

Allan, R. P., B. J. Soden, V. O. John, W. Ingram, and P. Good (2010), Current changes in tropical precipitation, *Environ. Res. Lett.*, *5*(2), 025205, doi:10.1088/1748-9326/5/2/025205.

Allen, R. G. (1998), *Crop Evapotranspiration: Guidelines for Computing Crop Water Requirements*, Food and Agriculture Organization of the United Nations, Rome.

Allen, R. G., M. Smith, A. Perrier, and L. S. Pereira (1994), An update for the calculation of reference evapotranspiration, *Int. Comm. Irrig. Drain. Bull.*, *43*, 35–92.

Alley, W. M. (1984), The Palmer Drought Severity Index: Limitations and assumptions, *J. Clim. Appl. Meteorol.*, *23*(7), 1100–1109.
Anav, A., G. Murray-Tortarolo, P. Friedlingstein, S. Sitch, S. Piao, and Z. Zhu (2013), Evaluation of land surface models in reproducing satellite derived leaf area index over the high-latitude northern hemisphere. Part II: Earth system models, *Remote Sens.*, *5*(8), 3637–3661, doi:10.3390/rs5083637.
Barichivich, J., K. Briffa, R. Myneni, G. Schrier, W. Dorigo, C. Tucker, T. Osborn, and T. Melvin (2014), Temperature and snow-mediated moisture controls of summer photosynthetic activity in northern terrestrial ecosystems between 1982 and 2011, *Remote Sens.*, *6*(2), 1390–1431, doi:10.3390/rs6021390.
Boening, C., J. K. Willis, F. W. Landerer, R. S. Nerem, and J. Fasullo (2012), The 2011 La Niña: So strong, the oceans fell, *Geophys. Res. Lett.*, *39*, L19602, doi:10.1029/2012GL053055.
Bonsal, B. R., and R. G. Lawford (1999), Teleconnections between El Niño and La Niña events and summer extended dry spells on the Canadian Prairies, *Int. J. Climatol.*, *19*(13), 1445–1458.
Burke, E. J., S. J. Brown, and N. Christidis (2006), Modeling the recent evolution of global drought and projections for the twenty-first century with the Hadley Centre Climate Model, *J. Hydrometeorol.*, *7*(5), 1113–1125, doi:10.1175/JHM544.1.
Chou, C., C. A. Chen, P. H. Tan, and K. T. Chen (2011), Mechanisms for global warming impacts on precipitation frequency and intensity, *J. Clim.*, *25*(9), 3291–3306, doi:10.1175/JCLI-D-11-00239.1.
Cleugh, H. A., R. Leuning, Q. Mu, and S. W. Running (2007), Regional evaporation estimates from flux tower and MODIS satellite data, *Remote Sens. Environ.*, *106*(3), 285–304, doi:10.1016/j.rse.2006.07.007.
Dai, A. (2011), Characteristics and trends in various forms of the Palmer Drought Severity Index during 1900–2008, *J. Geophys. Res.*, *116*, D12115, doi:10.1029/2010JD015541.
Dai, A., I. Y. Fung, and A. D. DelGenio (1997), Surface observed global land precipitation variations during 1900–88, *J. Clim.*, *10*(11), 2943–2962.
Dai, A., K. E. Trenberth, and T. Qian (2004), A global dataset of Palmer Drought Severity Index for 1870–2002: Relationship with soil moisture and effects of surface warming, *J. Hydrometeorol.*, *5*(6), 1117–1130, doi:10.1175/JHM-386.1.
Gerten, D., S. Rost, W. von Bloh, and W. Lucht (2008), Causes of change in 20th century global river discharge, *Geophys. Res. Lett.*, *35*, L20405, doi:10.1029/2008GL035258.
Gu, G., R. F. Adler, G. J. Huffman, and S. Curtis (2007), Tropical rainfall variability on interannual-to-interdecadal and longer time scales derived from the GPCP monthly product, *J. Clim.*, *20*(15), 4033–4046, doi:10.1175/JCLI4227.1.
Guttman, N. B., J. R. Wallis, and J. R. M. Hosking (1992), Spatial comparability of the Palmer Drought Severity Index, *J. Am. Water Resour. Assoc.*, *28*(6), 1111–1119.
Hall, F. G., E. Brown de Colstoun, G. J. Collatz, D. Landis, P. Dirmeyer, A. Betts, G. J. Huffman, L. Bounoua, and B. Meeson (2006), ISLSCP Initiative II global data sets: Surface boundary conditions and atmospheric forcings for land-atmosphere studies, *J. Geophys. Res.*, *111*, D22S01, doi:10.1029/2006JD007366.
Harris, I., P. D. Jones, T. J. Osborn, and D. H. Lister (2013), Updated high-resolution grids of monthly climatic observations—The CRU TS3.10 dataset, *Int. J. Climatol.*, doi:10.1002/joc.3711.
Heim, R. R. (2002), A review of twentieth-century drought indices used in the United States, *Bull. Am. Meteorol. Soc.*, *83*(8), 1149–1165.
Hobbins, M. T., A. Dai, M. L. Roderick, and G. D. Farquhar (2008), Revisiting the parameterization of potential evaporation as a driver of long-term water balance trends, *Geophys. Res. Lett.*, *35*, L12403, doi:10.1029/2008GL033840.
Huntington, T. G. (2006), Evidence for intensification of the global water cycle: Review and synthesis, *J. Hydrol.*, *319*(1-4), 83–95, doi:10.1016/j.jhydrol.2005.07.003.
Ichii, K., M. Kondo, Y. Okabe, M. Ueyama, H. Kobayashi, S.-J. Lee, N. Saigusa, Z. Zhu, and R. Myneni (2013), Recent changes in terrestrial gross primary productivity in Asia from 1982 to 2011, *Remote Sens.*, *5*(11), 6043–6062, doi:10.3390/rs5116043.
Impens, I., and R. Lemeur (1969), Extinction of net radiation in different crop canopies, *Theor. Appl. Climatol.*, *17*(4), 403–412.
Jones, P. D., D. H. Lister, T. J. Osborn, C. Harpham, M. Salmon, and C. P. Morice (2012), Hemispheric and large-scale land-surface air temperature variations: An extensive revision and an update to 2010, *J. Geophys. Res.*, *117*, D05127, doi:10.1029/2011JD017139.
Jung, M., et al. (2010), Recent decline in the global land evapotranspiration trend due to limited moisture supply, *Nature*, *467*(7318), 951–954, doi:10.1038/nature09396.
Karl, T. R. (1986), The Sensitivity of the Palmer Drought Severity Index and Palmer's Z-index to their calibration coefficients including potential evapotranspiration, *J. Clim. Appl. Meteorol.*, *25*, 77–86.
Kelliher, F. M., R. Leuning, M. R. Raupach, and E. D. Schulze (1995), Maximum conductances for evaporation from global vegetation types, *Agric. For. Meteorol.*, *73*(1–2), 1–16.
Liu, C., and R. P. Allan (2013), Observed and simulated precipitation responses in wet and dry regions 1850–2100, *Environ. Res. Lett.*, *8*(3), 034002, doi:10.1088/1748-9326/8/3/034002.
Lockwood, J. G. (1999), Is potential evapotranspiration and its relationship with actual evapotranspiration sensitive to elevated atmospheric CO_2 levels?, *Clim. Change*, *41*(2), 193–212, doi:10.1023/A:1005469416067.
Miralles, D. G., et al. (2014), El Niño–La Niña cycle and recent trends in continental evaporation, *Nat. Clim. Change*, *4*(2), 122–126, doi:10.1038/nclimate2068.
Monteith, J. L. (1965), Evaporation and the environment, *Symp. Soc. Exp. Biol.*, *19*, 205–234.
New, M., M. Hulme, and P. Jones (2000), Representing twentieth-century space–time climate variability. Part II: Development of 1901–96 monthly grids of terrestrial surface climate, *J. Clim.*, *13*(13), 2217–2238.
Osborn, T. J., and P. D. Jones (2014), The CRUTEM4 land-surface air temperature data set: Construction, previous versions and dissemination via Google Earth, *Earth Syst. Sci. Data*, *6*(1), 61–68, doi:10.5194/essd-6-61-2014.
Palmer, W. C. (1965), Meteorological drought, U.S. Weather Bureau Research Paper 45, U.S. Dep. of Commerce, Washington, D. C.
Priestley, C. H., and R. J. Taylor (1972), Assessment of surface heat-flux and evaporation using large-scale parameters, *Mon. Weather Rev.*, *100*(2), 81–92.
Qian, Y., D. Gong, J. Fan, L. R. Leung, R. Bennartz, D. Chen, and W. Wang (2009), Heavy pollution suppresses light rain in China: Observations and modeling, *J. Geophys. Res.*, *114*, D00K02, doi:10.1029/2008JD011575.
Reichle, R. H., R. D. Koster, G. J. M. De Lannoy, B. A. Forman, Q. Liu, S. P. P. Mahanama, and A. Touré (2011), Assessment and enhancement of MERRA land surface hydrology estimates, *J. Clim.*, *24*(24), 6322–6338, doi:10.1175/JCLI-D-10-05033.1.
Rienecker, M. M., et al. (2011), MERRA: NASA's modern-era retrospective analysis for research and applications, *J. Clim.*, *24*(14), 3624–3648, doi:10.1175/JCLI-D-11-00015.1.
Sheffield, J., K. M. Andreadis, E. F. Wood, and D. P. Lettenmaier (2009), Global and continental drought in the second half of the 20th century: Severity-area-duration analysis and temporal variability of large-scale events, *J. Clim.*, *22*, 1962–1981, doi:10.1175/2008JCLI2722.1.

Sheffield, J., E. F. Wood, and M. L. Roderick (2012), Little change in global drought over the past 60 years, *Nature*, *491*(7424), 435–438, doi:10.1038/nature11575.

Shiu, C.-J., S. C. Liu, C. Fu, A. Dai, and Y. Sun (2012), How much do precipitation extremes change in a warming climate?, *Geophys. Res. Lett.*, *39*, L17707, doi:10.1029/2012GL052762.

Shuttleworth, W. J. (1993), Evaporation, in *Handbook of Hydrology*, edited by D. R. Maidment, pp. 4.1–4.53, McGraw-Hill, New York.

Thornthwaite, C. W. (1948), An approach toward a rational classification of climate, *Geogr. Rev.*, *38*(1), 55–94.

Thornthwaite, C. W., and J. R. Mather (1955), *The Water Balance*, 104 pp., Drexel Institute of Technology, Centerton, New Jersey.

Trenberth, K. E., A. Dai, G. van der Schrier, P. D. Jones, J. Barichivich, K. R. Briffa, and J. Sheffield (2014), Global warming and changes in drought, *Nat. Clim. Change*, *4*(1), 17–22, doi:10.1038/nclimate2067.

van der Schrier, G., P. D. Jones, and K. R. Briffa (2011), The sensitivity of the PDSI to the Thornthwaite and Penman-Monteith parameterizations for potential evapotranspiration, *J. Geophys. Res.*, *116*, D03106, doi:10.1029/2010JD015001.

van der Schrier, G., J. Barichivich, K. R. Briffa, and P. D. Jones (2013), A scPDSI-based global data set of dry and wet spells for 1901–2009, *J. Geophys. Res. Atmos.*, *118*, 4025–4048, doi:10.1002/jgrd.50355.

Vicente-Serrano, S. M., J. I. López-Moreno, L. Gimeno, R. Nieto, E. Morán-Tejeda, J. Lorenzo-Lacruz, S. Beguería, and C. Azorin-Molina (2011), A multiscalar global evaluation of the impact of ENSO on droughts, *J. Geophys. Res.*, *116*, D20109, doi:10.1029/2011JD016039.

Wang, K., J. Mao, R. Dickinson, X. Shi, W. Post, Z. Zhu, and R. Myneni (2013), Evaluation of CLM4 solar radiation partitioning scheme using remote sensing and site level FPAR datasets, *Remote Sens.*, *5*(6), 2857–2882, doi:10.3390/rs5062857.

Wells, N., S. Goddard, and M. J. Hayes (2004), A self-calibrating Palmer Drought Severity Index, *J. Clim.*, *17*(12), 2335–2351.

Wentz, F. J., L. Ricciardulli, K. Hilburn, and C. Mears (2007), How much more rain will global warming bring?, *Science*, *317*(5835), 233–235, doi:10.1126/science.1140746.

Wolter, K., and M. S. Timlin (1998), Measuring the strength of ENSO events: How does 1997/98 rank?, *Weather*, *53*(9), 315–324, doi:10.1002/j.1477-8696.1998.tb06408.x.

Wolter, K., and M. S. Timlin (2011), El Niño/Southern Oscillation behaviour since 1871 as diagnosed in an extended multivariate ENSO index (MEI.ext), *Int. J. Climatol.*, *31*(7), 1074–1087, doi:10.1002/joc.2336.

Yan, H., and H. H. Shugart (2010), An air relative-humidity-based evapotranspiration model from eddy covariance data, *J. Geophys. Res.*, *115*, D16106, doi:10.1029/2009JD013598.

Yan, H., et al. (2012), Global estimation of evapotranspiration using a leaf area index-based surface energy and water balance model, *Remote Sens. Environ.*, *124*, 581–595, doi:10.1016/j.rse.2012.06.004.

Yan, H., Q. Yu, Z. C. Zhu, R. B. Myneni, H. M. Yan, S. Q. Wang, and H. H. Shugart (2013), Diagnostic analysis of interannual variation of global land evapotranspiration over 1982–2011: Assessing the impact of ENSO, *J. Geophys. Res. Atmos.*, *118*, 8969–8983, doi:10.1002/jgrd.50693.

Yi, Y., J. S. Kimball, L. A. Jones, R. H. Reichle, and K. C. McDonald (2011), Evaluation of MERRA land surface estimates in preparation for the soil moisture active passive mission, *J. Clim.*, *24*(15), 3797–3816, doi:10.1175/2011JCLI4034.1.

Zhao, X., et al. (2013), The Global Land Surface Satellite (GLASS) remote sensing data processing system and products, *Remote Sens.*, *5*(5), 2436–2450, doi:10.3390/rs5052436.

Zhou, L., et al. (2014), Widespread decline of Congo rainforest greenness in the past decade, *Nature*, *509*(7498), 86–90, doi:10.1038/nature13265.

Zhu, Z., J. Bi, Y. Pan, S. Ganguly, A. Anav, L. Xu, A. Samanta, S. Piao, R. Nemani, and R. Myneni (2013), Global data sets of vegetation Leaf Area Index (LAI)3 g and Fraction of Photosynthetically Active Radiation (FPAR)3 g derived from Global Inventory Modeling and Mapping Studies (GIMMS) Normalized Difference Vegetation Index (NDVI3g) for the period 1981 to 2011, *Remote Sens.*, *5*(2), 927–948, doi:10.3390/rs5020927.